공학석사학위논문

A Characterization of Shale Gas Reservoir Using Fast Marching Method Combined With Model Selection Approach

Fast Marching Method와 모델선정법을 이용한 셰일가스 저류층 특성화

2015년 2월

서울대학교 대학원
에너지시스템공학부
박 지 혜

Abstract

A Characterization of Shale Gas Reservoir Using Fast Marching Method Combined With Model Selection Approach

Ji-hye Park

Department of Energy Systems Engineering

The Graduate School

Seoul National University

Shale gas reservoirs show various production profiles depending on methods of hydraulic fracturing. Characterization for given shale gas reservoir is essentially included to predict future performances. Clustering of various reservoir models by their similarities and selecting of a cluster similar to the production history data are introduced in the process of characterization. The conventional clustering method using static properties such as fracture half-lengths and mean permeability has shown limited capability for realistic characteristics of a shale gas reservoir.

In this study, the Fast Marching Method (FMM) combined with a model selection approach is proposed to develop reservoir models showing similar production profiles with the history data. The stimulated reservoir volume (SRV) is obtained from FMM as a value of the similarity in order to reflect the dynamic connectivity.

The method is applied to various shale gas reservoirs with different fracture geometries for verification. It effectively gathers models with similar production profiles and fracture distributions. The accuracy of Estimated Ultimate Recovery (EUR) prediction is improved up to 7-14%p compared to the conventional method.

Table of Contents

List of Tables

List of Figures

1. Introduction

As the world's conventional oil and gas fields are been depleted, unconventional resources, such as shale gas and shale oil, have taken a significant share of the U.S. energy supply and the world energy market (Holditch, 2010). **Figure 1.1** shows the locations of major shale gas plays in the U.S. and **Table 1.1** compares the key characteristic for five key shale gas plays.

Shale gas is natural gas produced from shale formations. For producing shale gas, horizontal drilling with hydraulic fracturing that increases both drainage volume and fracture permeability of the shale formation is essential owing to the low permeability of the shale formation in the range between micro-Darcy and nano-Darcy.
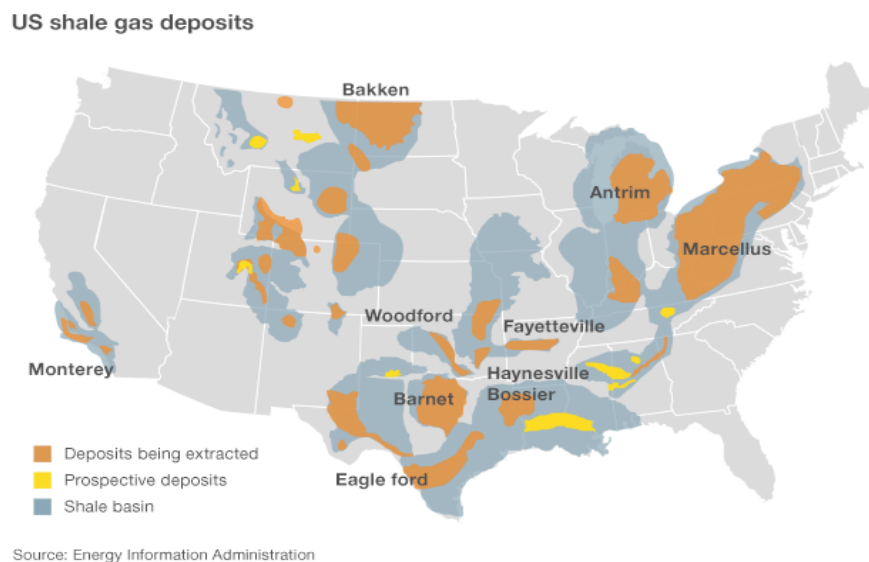
Figure 1.1 Locations of major shale gas plays in the U.S. (David, 2013).

Table 1.1 Summary of the key characteristic for five key shale gas plays in the U.S. (Dong et al., 2014)

Shale gas play	Eagle Ford	Barnett	Marcellus	Fayetteville	Haynesville
Area, acres	3,000,000	3,200,000	15,000,000	2,560,000	5,760,000
Depth, ft	5,500–14,400	6,500–8,500	3,300–8,800	1,200–8,000	10,000–14,000
Net pay, ft	3–326	100–600	45–384	50–325	200–300
Porosity, %	3–12	4–5	3–13	2–8	8–14
System permeability, 10-3 md	0.1–0.7	0.07–5	0.2–0.9	1–4	0.5–400
Initial production rate, MMscf/day	6.0	1.2–4.7	7.7	2.2	10
Average lateral length, ft	5,600	4,000	3,700	4,800	4,600
Well spacing, acres/well	147	111	104	129	124

However, the uncertainty of fracture half-length, permeability within the enhanced region and their associated properties make it necessary to not just develop a single realization but multiple realizations of the reservoir. To do this, it is essential to utilize history matching which selects best-fit models for the reservoir showing similar performance to field production data. The inherent assumption is that if modeled results is matched with the field data, the model is deemed to be a most similar reservoir and is used to predict future production.

Traditional history matching methods have a model perturbation step. They update prior reservoir model until the difference between the simulated production data and the field production data is minimized below certain tolerance. The disadvantage of the method is that the complicated relationship between static and dynamic variables and the large number of equations involved make history matching difficult. Another disadvantage is that inverse problem is strongly nonlinear. If an initial model is far from the real field, an optimization algorithm might fail to find the global minimum and converge to local minimum. Non-gradient methods such as genetic algorithm or simulated annealing theoretically ensure to spot a global minimum, but are computationally prohibitive (Park, 2014).

Model selection algorithm, which is utilized in this thesis, is not a model perturbation process. The method deals with the model as a whole, and evaluates whether the characteristics exhibited by it are similar to other models within a cluster. Then, the history data is then used to select the group that exhibits production performance closest to the history data. To sum up, it is a selection of a group showing similar response to the history data.

Once the initial reservoir models have been created, they have to be analyzed in order to assess their characteristics. This can be achieved by using a numerical simulation or by using a faster simulation technique, such as streamline simulation. For

my thesis, Fast Marching Method (FMM) is utilized to rapidly assess stimulated reservoir volume (SRV) of initial suite of reservoir models so that we can begin dividing the models into groups that exhibit similar characteristic.

Yin et al. (2011) introduced FMM for computing well drainage volume for shale gas wells with multistage fractures and calibrated the shale gas reservoir model by matching the drainage volume with the SRV acquired from an independent source.

Xie et al. (2012) proposed the methodology for shale gas reservoir model calibration by applying of FMM. They combined FMM with genetic algorithm. After obtaining calibrated parameters, they estimated SRV where the first plateau in the drainage volume plot.

After assessing SRV of the models, distance-based clustering has to be performed for calculating distance between pairs of models, dividing into distinct groups or clusters based on the distance, such that models grouped together show similar characteristics and selecting the representative models.

Suzuki and Caers (2008) applied Hausdorff distance to channelized reservoir for grouping the reservoirs and selecting the representative models because they thought the distribution of sand facies had effect on production performance. Hausdorff distance measures the similarity of shape between models.

Scheidt and Caers (2009) proposed a distance as Eq. (1.1). The distance was defined as the differences of field oil production rates acquired from streamline simulation. The representative models were selected among clusters showing similar production rate. They validated their method by applying to conventional oil reservoir.

$$\delta_{ij} = \sum_{t \in \{10000,\ 20000\}} \left| FOPR_i^{streamline}(t) - FOPR_j^{streamline}(t) \right| \tag{1.1}$$

Jin (2011) proposed a distance for oilsand reservoir as difference between substitutive models composed of the region of steam passed and non-passed using streamline simulation.

Zhang and Fassihi (2013) applied distance-based clustering to shale oil history matching scheme. Among 40 reservoir models selected from genetic algorithm, reservoir models were grouped according to the distance as shown in Eq. (1.2). The distance is consist of static parameters, such as porosity and saturation.

$$\sqrt{(\phi_2 - \phi_1)^2 + (S_{w2} - S_{w1})^2 + \cdots + (PERMX_2 - PERMX_1)^2} \tag{1.2}$$

After completing the distance-based clustering, model selection is performed to select reservoir models showing the similar trend of history data.

Bhowmik et al. (2010) predicted the migration of CO_2 plume using a distance-metric approach to reservoir-model selection. The flow characteristics of the models were assessed using random walker simulation. Based on the characteristics, the models were divided into several clusters using k-means clustering algorithm and representative models are picked. Once the representative models were run through the flow simulator, the group which shows similar trend to injection well data was selected and predicted CO_2 migration with the models in the final group.

Singh and Srinivasan (2013) analyzed economic uncertainty with 4 reservoir models selected from model selection, the same procedure of Bhowmik et al. (2010).

The limitation of previous studies are as follows.

1) Even though it has been widely researched about shale gas, a study of shale gas reservoir characterization is deficient. Since shale gas shows various production profile according to hydraulic fracturing, the need of reservoir characterization has been increased for reliable future prediction.

2) For defining distance in order to group the initial models, static parameters, e.g. permeability, saturation, can hardly depict shale gas reservoir performance because it cannot reflect dynamic connectivity of reservoir.

3) There is no application of FMM combined with model selection approach to shale gas reservoirs.

The main objective of this study is to propose a new methodology of shale gas reservoir characterization using FMM combined with model selection approach. First, a new concept of distance which can reflect dynamic connectivity of reservoir using FMM is proposed. Second, representative models are chosen from each cluster based on the distance and performed model selection. Reservoir models with different fracture geometry are used to verify the proposed method.

This paper is composed of five chapters. Chapter 1 described the research trends and applications of FMM, distance-based clustering and model selection. Chapter 2 explains theoretical backgrounds in FMM, distance-based clustering and model selection. In chapter 3, the methodology is proposed to shale gas reservoir characterization using FMM combined with model selection. Chapter 4 presents results of reservoir characterization and comparison with conventional method. Chapter 5 summarizes and concludes the thesis. Finally, Appendix A is the results of the proposed method to the shale gas reservoirs with different fracture distributions.

2. Theoretical Background

2.1 FMM(Fast Marching Method)

FMM (Sethian, 1996) is the method that can solve efficiently the Eikonal equation shown on Eq. (2.1). This method is often used in various fields such as seismic wave interpretation or fluid mechanics because it can track how wave or pressure propagates (Sethian and Vladimirsky, 2000). In Eq. (2.1), $F(\vec{x})$ is velocity at each location, while $T(\vec{x})$ is diffusive time of flight (DTOF). Velocity function $F(\vec{x})$ is always greater than or equal to zero, which means that the pressure is transmitted in only one direction. Therefore, the pressure fronts pass through every grid only once. This being so, the calculation can be done quickly.

$$F(\vec{x})\left|\nabla T(\vec{x})\right| = 1 \qquad (2.1)$$

Initial condition: $\left. T \right|_{f(\vec{x})=0} = 0$.

The transient pressure response in a heterogeneous permeable medium is represented by the diffusion equation (Eq. (2.2)) and can be derived into an Eikonal equation form through asymptotic method. Asymptotic method approximates the solution of equation to the most influential term when the solution is expressed as the sum of infinite terms. After Fourier transformation of Eq. (2.2), the equation is expressed as Eq. (2.3) in the frequency domain, while asymptotic solution, as shown in

Eq. (2.4), is expressed as the sum of infinite $A_k(\vec{x})$ values that represent pressure amplitude (Vasco et al., 2000). Note that the initial few terms of asymptotic solution have a major influence on the result. Only the solution shown as Eq. (2.5) when k equals 0 needs to be considered, as it represents the first pressure front to arrive. After inserting Eq. (2.5) into Eq. (2.3), pressure diffusion is represented in an Eikonal equation form as shown in Eq. (2.6). Here, hydraulic diffusivity ($\alpha(\vec{x})$) can be determined by Eq. (2.7) and depends on permeability ($k(\vec{x})$), porosity ($\phi(\vec{x})$), fluid viscosity (μ) and total compressibility (c_t). DTOF ($\tau(\vec{x})$) is computed based on the hydraulic diffusivity assigned to each grid; smaller value results in an increased DTOF.

$$\phi(\vec{x})\mu c_t \frac{\partial P(\vec{x},t)}{\partial t} = \nabla \bullet (k(\vec{x})\nabla P(\vec{x},t)) \tag{2.2}$$

$$\phi(\vec{x})\mu c_t(-iw)\tilde{P}(\vec{x},w) = k(\vec{x})\nabla^2 \tilde{P}(\vec{x},w) + \nabla k(\vec{x}) \bullet \nabla \tilde{P}(\vec{x},w) \tag{2.3}$$

$$\tilde{P}(\vec{x},w) = e^{-\sqrt{-iw\tau}(\vec{x})}\sum_{k=0}^{\infty}\frac{A_k(\vec{x})}{(\sqrt{-iw})^k} \tag{2.4}$$

$$\tilde{P}(\vec{x},w) = A_0(\vec{x})e^{-\sqrt{-iw\tau}(\vec{x})} \tag{2.5}$$

$$\sqrt{\alpha(\vec{x})}\left|\nabla \tau(\vec{x})\right| = 1 \tag{2.6}$$

$$\alpha(\vec{x}) = \frac{k(\vec{x})}{\phi(\vec{x})\mu c_t} \tag{2.7}$$

where

$\phi(\vec{x})$: *porosity, fraction*

μ : *gas viscosity, cp*

c_t : *total compressibility, psia^{-1}*

$P(\vec{x}, t)$: *pressure, psia*

$k(\vec{x})$: *permeability, md*

w : *time in Fourier domain*

$\tilde{P}(\vec{x}, w)$: *pressure in Fourier domain, psia*

$\tau(\vec{x})$: *diffusive time of flight(DTOF), day$^{1/2}$*

$A_k(\vec{x})$: *pressure amplitude*

$\alpha(\vec{x})$: *hydraulic diffusivity, ft^2/day.*

In the case of 2-dimensional orthogonal grids, Eq. (2.6) can be expressed as finite difference method, Eq. (2.8) (Sethian 1996). Here, D is the gradient operator that is

$$D_{ij}^{-x}\tau = (\tau_{i,j} - \tau_{i-1,j})/\Delta x \quad , \quad D_{ij}^{+x}\tau = (\tau_{i+1,j} - \tau_{i,j})/\Delta x \quad \text{in} \quad \text{x-direction,}$$

$D_{ij}^{-y}\tau = (\tau_{i,j} - \tau_{i,j-1})/\Delta y$, $D_{ij}^{+y}\tau = (\tau_{i,j+1} - \tau_{i,j})/\Delta y$ in y-direction, and max function tends to let pressure diffuse in one direction only.

For example, when assuming the pressure diffuses from the blue point in **Figure 2.1** and determining the DTOF of point A, the DTOF value of the blue point is 0, while the points around the point A have infinite DTOF values because the pressure has not been diffused yet. The DTOF at the point A can be determined using Eq. (2.9). Determining DTOF using Eq. (2.10), rearranged form of Eq. (2.9), takes less time than numerical analysis, which attains results through iteration.

$$\max(D_{ij}^{-x}\tau, -D_{ij}^{+x}\tau, 0) + \max(D_{ij}^{-y}\tau, -D_{ij}^{+y}\tau, 0) = \frac{1}{\alpha(\vec{x})} \tag{2.8}$$

$$\max\left(\left(\frac{\tau_a - 0}{\Delta x}\right), -\left(\frac{\infty - \tau_a}{\Delta x}\right), 0\right)^2 + \max\left(\left(\frac{\tau_a - \infty}{\Delta y}\right), -\left(\frac{\infty - \tau_a}{\Delta y}\right), 0\right)^2 = \frac{1}{\alpha_a} \tag{2.9}$$

$$\left(\frac{\tau_a - 0}{\Delta x}\right)^2 + 0 = \frac{1}{\alpha_a} \tag{2.10}$$

where

Δx : *x-length of a grid block, ft*

Δy : *y-length of a grid block, ft.*

Figure 2.2 is an illustration of the fundamental processes of FMM in a 2-dimensional orthogonal grid, and the grids are divided into three groups: 'accepted', 'neighbor' and 'far-away.' 'Accepted' grids have known values, 'neighbor' grids are located near 'accepted' grids and 'far-away' grids are the rest. DTOF of each grid is computed as shown below (Xie, 2012).

1) The red point in **Figure 2.2** a), which represents the production well, has DTOF of zero.

2) Compute the DTOF of 'neighbor' grids (point A, B, C, D of **Figure 2.2** b)) using finite difference method.

3) The grid with the smallest DTOF among the 'neighbor' grids (point A of **Figure 2.2** c)) is added to 'accepted' grids.

4) The grids (point E, F, G of **Figure 2.2** d)) near the grid that has just become 'accepted' are now added to 'neighbor' grids.

5) Repeat steps from 2) to 4) until all the points in the area become 'accepted.'
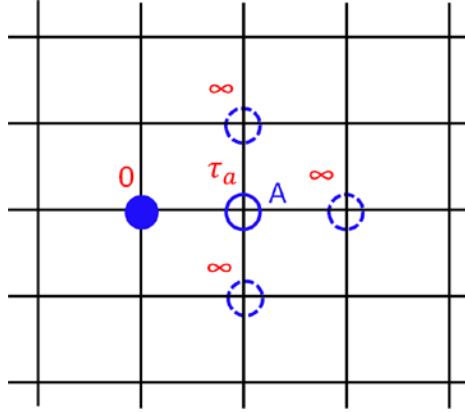
Figure 2.1 Illustration of two dimensional order finite difference calculation.
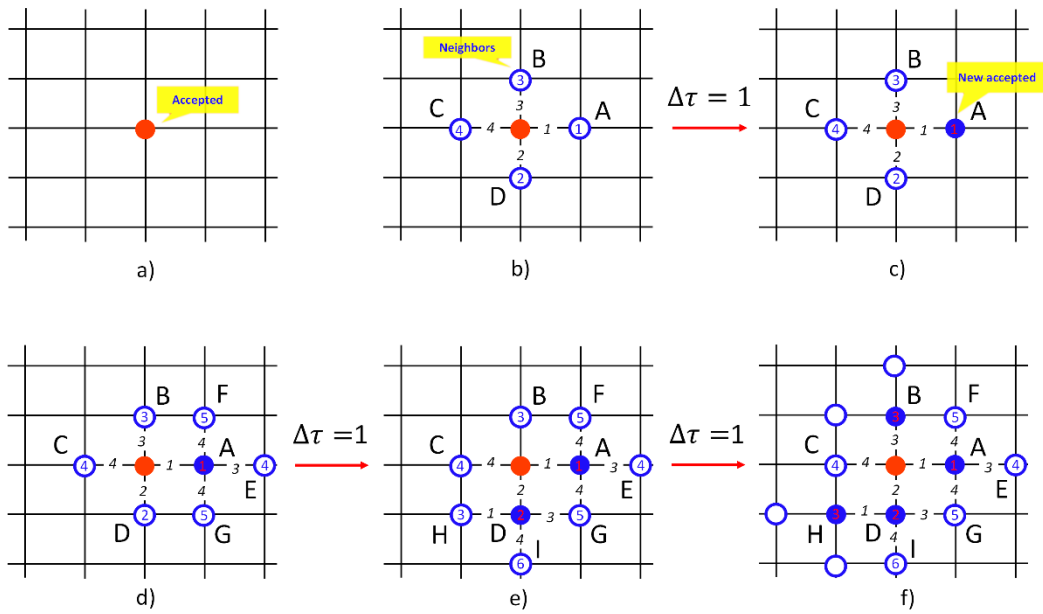
Figure 2.2 Illustration of FMM.

DTOF is the arrival time of pressure front propagation which can be obtained by applying FMM. The dimension of DTOF is square root of time and it depends on reservoir and fluid properties. There is a relation between DTOF and actual physical time shown as Eq. (2.11) and constant c is a geometric factor related to the flow pattern. For instance, in cases of linear, radial, and spherical flow, c is 2, 4, and 6 respectively (Kim et al., 2009). In this study, c is assumed as 6 while computing physical time.

$$t(\vec{x}) = \frac{\tau^2(\vec{x})}{c} \tag{2.11}$$

where

c : geometric factor, dimensionless.

Figure 2.3 shows DTOF for a 2-D in a homogeneous reservoir. DTOF gets bigger near red area and smaller near blue one. Figure 2.3 a) shows how pressure propagates radially when vertical well exists. Figure 2.3 b) is a case including one fracture in vertical well and it shows pressure front propagation happening while the fracture maintains its form at the same time. The permeability field for heterogeneous case is shown in **Figure 2.4** a). Permeability gets higher value in red area and lower in blue one. DTOF for heterogeneous case shown in Figure 2.4 b), shows the pressure front propagation progresses to north-eastwards first where the permeability is higher.
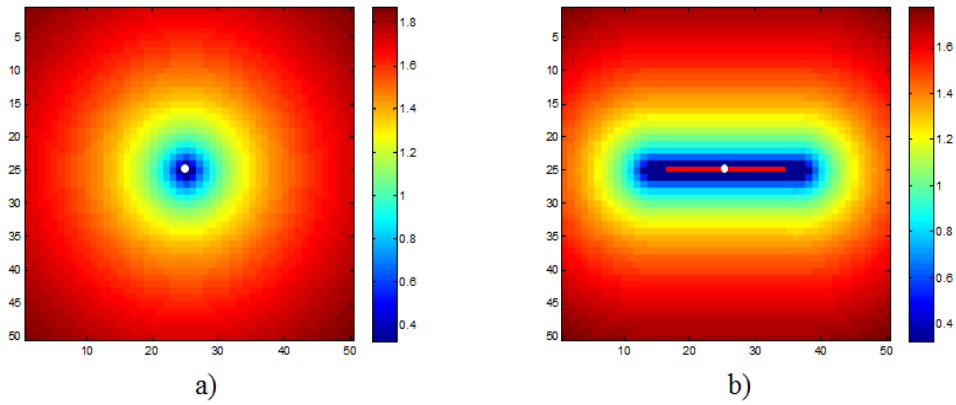
Figure 2.3 Top view of homogeneous reservoir: arrival time of a) vertical well, and

b) vertical well with a fracture.
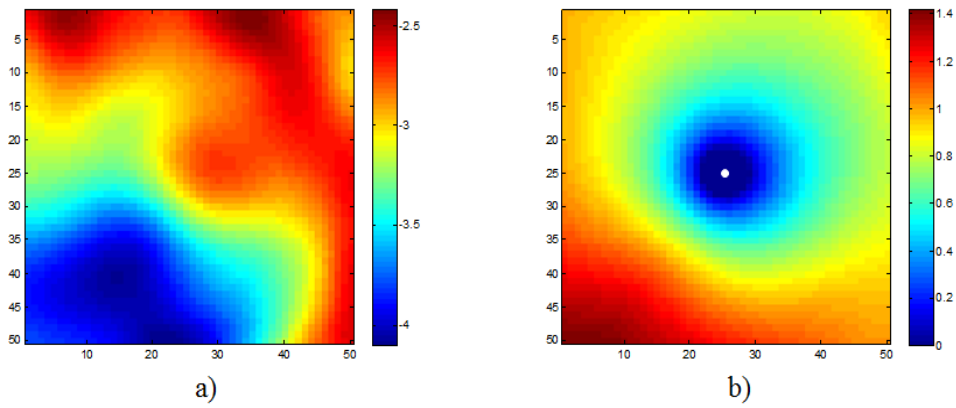
Figure 2.4 Top view of heterogeneous reservoir: a) permeability field (log scale),

and b) arrival time of vertical well (days).

When the pressure front arrives at a certain grid, it indicates that this grid is starting to be drained. In other words, all the grids which have smaller arrival time than considered have already been drained. Therefore, the drainage volume (V_p) at any time can easily be calculated by Eq. (2.12), summing up the pore volumes of the grids within that time contour.

$$V_p(t) = \sum_{i=1}^{N_{cells}} Cell\ Pore\ Volume\ (where\ t_i < t) \tag{2.12}$$

SRV can be estimated through drainage volume. Due to the characteristic that the permeability within the SRV are generally higher than that of the matrix, DTOF in SRV is smaller compared to the matrix. Therefore the drainage volume at the point where the gradient sharply decreases can be regarded as the SRV.

Figure 2.5 a) is a schematic diagram of the single fractured heterogeneous reservoir. The reservoir is characterized with three permeability regions: the fracture permeability (red, 1 md), the enhanced permeability (green, 10-3−10-4 md) near the fracture and the matrix permeability (blue, 3E-5−3E-6 md). Figure 2.5 b) shows DTOF of each grid and DTOF has high value in a red grid, and low value in the blue one. **Figure 2.6** indicates drainage volume calculated with DTOF at the reservoir. At approximately 1000th day, the curve flattens out which indicates that the pressure has reached the matrix. The drainage volume at this time is essentially corresponding to the SRV. The drainage volume reaches the reservoir pore volume when the slope converges to 0.
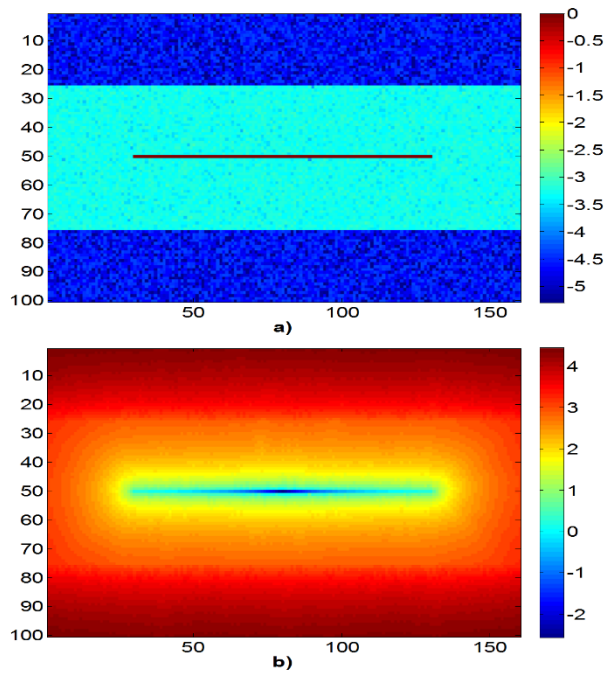
Figure 2.5 Top view of heterogeneous reservoir with single fracture:

a) permeability field, and b) arrival time of pressure front (days).
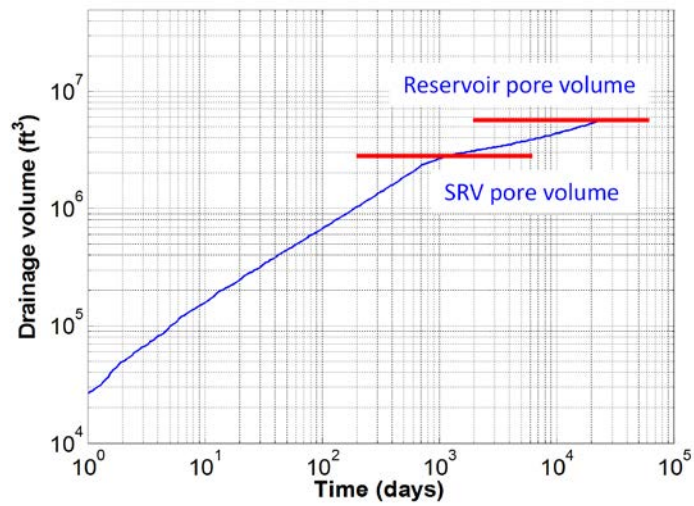
Figure 2.6 Drainage volume versus time for a single fracture reservoir

(log-log scale).

16

2.2 Distance-based clustering

Distance-based clustering is consist of the calculation of distance which represents dissimilarities of models and the application of clustering. The distance is a quantitative measure of differences between each model. A distance can be calculated in any manner, as long as it is correlated to the flow response of interest (Schedit and Caers, 2009).

2.2.1 Multi-dimensional scaling

Multidimensional scaling (MDS) is a means of visualizing the level of similarity of individual objects from many kinds of distance or dissimilarity metrics and can produce a representation of the objects in a small number of dimensions. Generally, a distance between N objects is the measurement of dissimilarity, $d_{ij}, i, j = 1,...,n$ and satisfies conditions as below (Park, 2000).

- The distance between two points is greater than 0.

- The distance between a point and itself is 0 and the distance between the different points is never 0.

- The distance between i and j is equal to the distance between j and i. ($d_{ij} = d_{ji}$)

- The sum of two sides of a triangle is always greater than the other side of it. ($d_{ij} + d_{jk} \geq d_{ik}$)

Dissimilarity matrix (D) is set using distances as shown in Eq. (2.13). A dissimilarity matrix is a symmetric matrix where diagonal elements is 0 (Choi, 2014).

$$D = \begin{bmatrix} 0 & d(x_1, x_2) & \cdots & d(x_1, x_{N-1}) & d(x_1, x_N) \\ d(x_2, x_1) & 0 & \cdots & \cdots & d(x_2, x_N) \\ \cdots & \cdots & 0 & \cdots & \cdots \\ d(x_{N-1}, x_1) & \cdots & \cdots & 0 & d(x_{N-1}, x_N) \\ d(x_N, x_1) & d(x_N, x_2) & \cdots & d(x_N, x_{N-1}) & 0 \end{bmatrix} \qquad (2.13)$$

where

x : a vector that represents one reservoir model

One method of defining the distance is Hausdorff distance representing similarity of two objects (Dubuisson and Jain, 1994). Eq. (2.16) is a definition of Hausdorff distance between set A and set B. It is the maximum value of Eq. (2.14) and Eq. (2.15). Here, a is any coordinates of points within A and b is the same. $d(a, b)$ is a Euclidean distance between a and b. Eq. (2.14) means the distance which has long value among small distances from any point in A to any point in B. Likewise, Eq. (2.15) means the distance which has long value among small distances from any point in B to any point in A.

$$d(A, B) = \max_{a \in A} \left\{ \min_{b \in B} \left\{ d(a, b) \right\} \right\} \qquad (2.14)$$

$$d(B, A) = \max_{b \in B} \left\{ \min_{a \in A} \left\{ d(b, a) \right\} \right\} \qquad (2.15)$$

$$H(A, B) = \max(d(A, B), d(B, A)) \qquad (2.16)$$

Figure 2.7 is the example of calculating Hausdorff distance. A has two points and B has three points. First, compute the distance between a_1 and b_j's and keep the shortest. Second, compute the distance between a_2 and b_j's and keep the shortest. Third, find the largest of the two distances ($d(a_1, b_2)$) and this is $d(A, B)$. Same procedure is used to compute $d(B, A)$. $d(B, A)$ is $d(b_3, a_2)$. In this case, $d(b_3, a_2)$, the maximum value among $d(A, B)$ and $d(B, A)$, is Hausdorff distance between A and B.

Figure 2.8 is dissimilarity matrix from calculated Hausdorff distance of initial reservoir models and MDS plane from the dissimilarity matrix. Similar objects are represented by points that are close to each other and dissimilar objects are represented by points that are far apart.
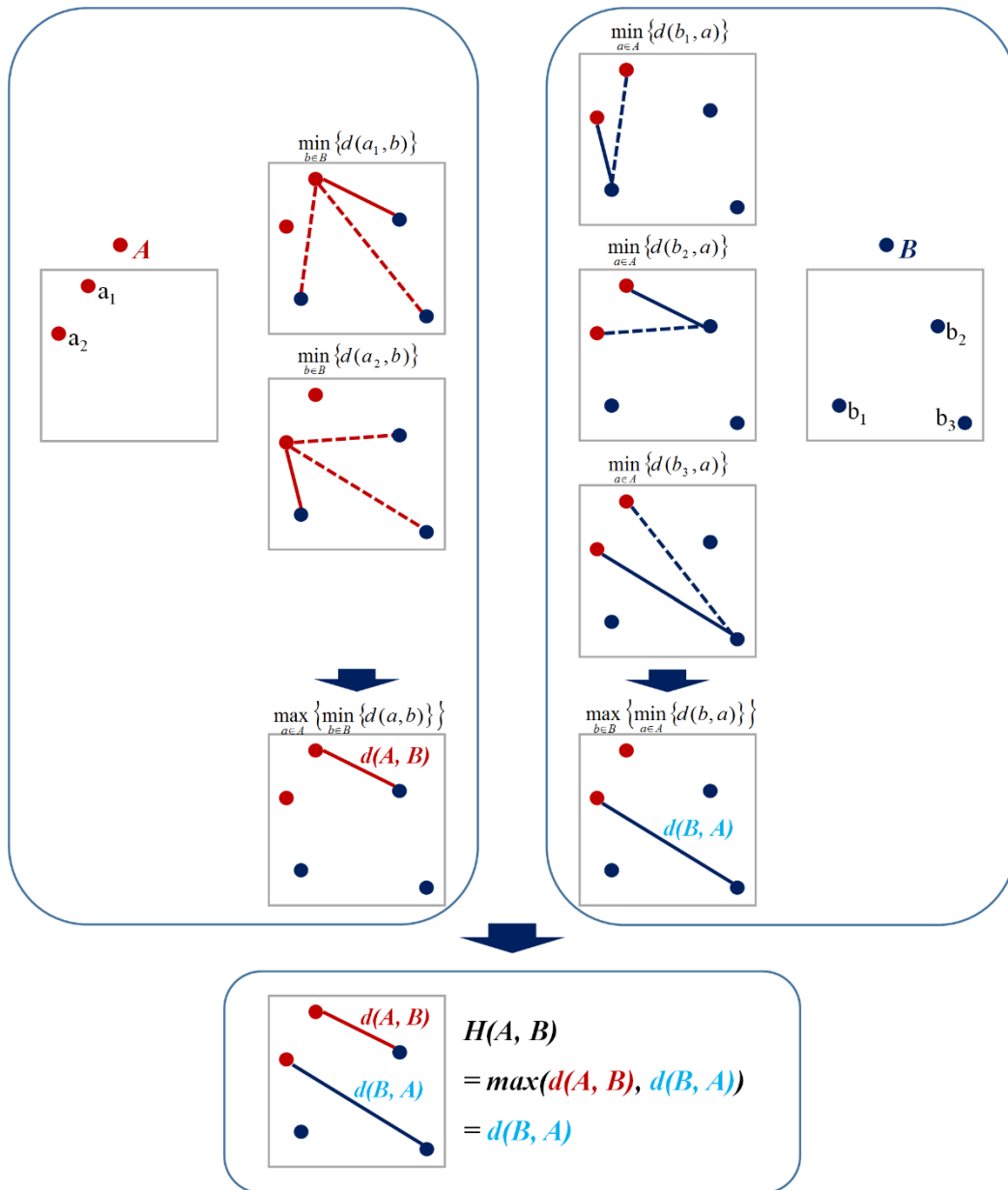
Figure 2.7 Example of Hausdorff distance (modified from Lee, 2014).

$$
D = \begin{bmatrix} 0 & H(1,2) & \cdots & H(1,N) \\ H(2,1) & \ddots & & H(2,N) \\ \vdots & & \ddots & \vdots \\ H(N,1) & H(N,1) & \cdots & 0 \end{bmatrix}
$$
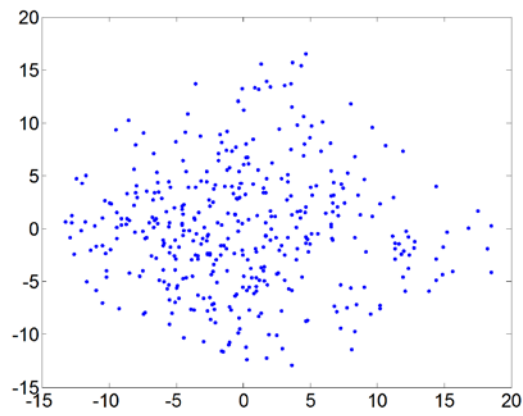
Figure 2.8 MDS from distance matrix.

2.2.2 K-means clustering

Clustering is a method of grouping a set of models in such a way that models in the same group are more similar to each other than to those in other groups. k-means clustering is widely used among several methods in clustering due to its ease of implementation. The goal of k-means clustering is to cluster n models to k groups. It is important to select cluster centers because models are assigned to the nearest cluster from the cluster center.

Figure 2.9 is the procedure of k-means clustering. The algorithm can be stated as follows (Caers, 2011):

1) Set k cluster centers randomly in the space.

2) Calculate the Euclidean distance of each point from the k centers.

3) Assign models to the closest centers.

4) Calculate new means of the assigned models to obtain new cluster centers.

5) Repeat steps 2 to 4 until there is no change in cluster centers.

However, this process has some drawbacks. The number of clusters has to be defined before carrying out k-means clustering and the optimization procedure of finding the cluster centers might converge to a local minimum. In order to resolve the problem of convergence to a local minimum, the process to find optimum cluster centers needs to be repeated a number of times with different starting cluster centers (Bhowmik, 2014).

In order to define the number of clusters, Bhowmik (2010)'s method is implemented as seen in Eq. (2.17). Bhowmik (2010) defines 'effectiveness of clustering', given as the ratio of sum of square distances of each data point from its cluster center to

the sum of square distances between cluster centroids:

$$\eta_k = \sum_{i=1}^{k} \sum_{j=1,\; j\,in\,i}^{m} d_{ij}^2 \bigg/ \sum_{i=1}^{k} \sum_{j=1,\; j\neq i}^{k} d_{ij}^2 \qquad (2.17)$$

where

η_k : effectiveness of clustering with k clusters

m : models in a particular cluster.

The purpose of clustering is to maximize the distances between cluster centers while minimizing the spread of objects within each cluster. Therefore, the lower η_k indicates better clustering. **Figure 2.10** shows the trend of η_k against the number of cluster (k). The value of η_k is decreasing as the number of clusters is increasing. The k where the slope is near 0 is the optimum number of cluster.
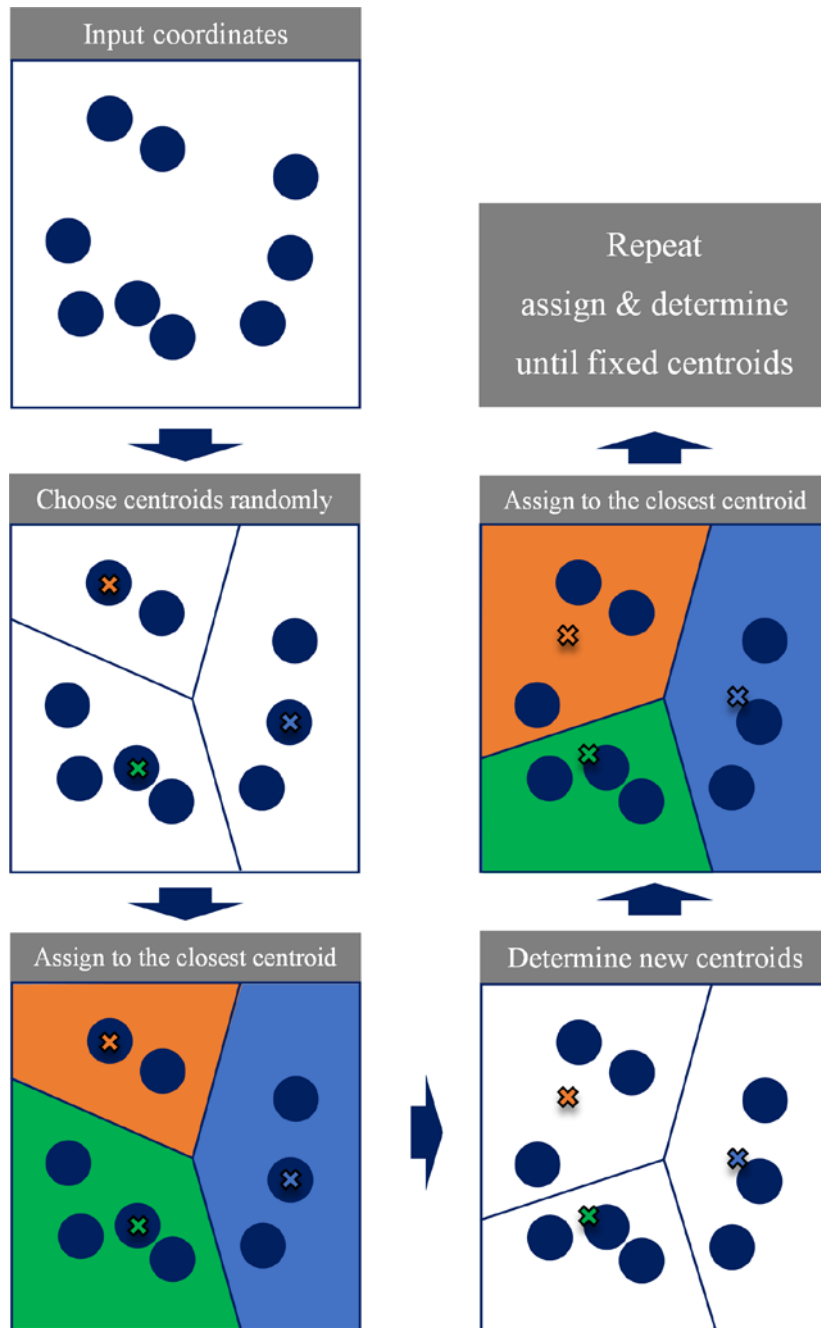
Figure 2.9 A Procedure of k-means clustering (modified from Lee, 2014).
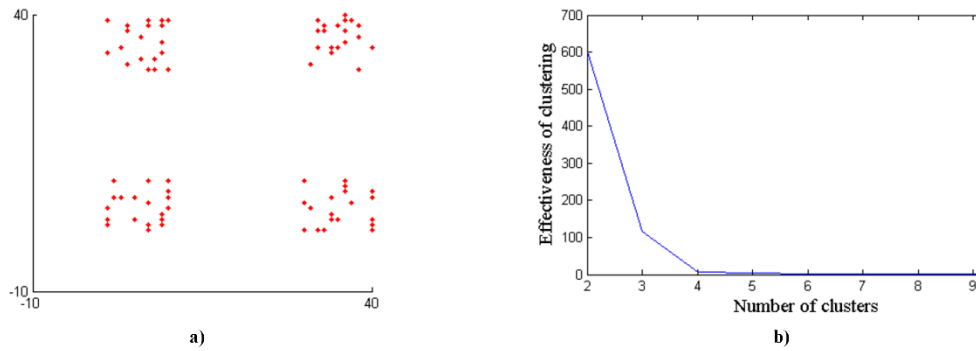
Figure 2.10 a) Actual data points used for the demonstration. There are clearly 4 clusters of points in this case. B) Plot of effectiveness of clustering vs number of clusters clearly shows a kink at 4, which is the correct number of clusters (Bhowmik, 2014).

2.3 Model selection algorithm

Once distance-based clustering is finished, representative models are picked from each cluster and run through a full-physics numerical simulator. The simulated responses are compared to the history data in other to find the model cluster closest to the history data. To quantify how similar simulated responses to history data, calculate posterior probability of the clusters. The following is the procedure of model selection (Mantilla, 2010).

1) Calculating prior probability of cluster m

All N models are equally probable before the model selection process because there is no other information about the models. Hence, Eq. (2.18) is the prior probability of cluster m.

$$P(z^m(u)) = \frac{Number \; of \; mo\,dels \; in \; cluster \; m}{Total \; number \; of \; mo\,dels} \tag{2.18}$$

2) Calculating likelihood function $P(RF_{ref}|z^m(u))$

The likelihood function can be calculated from simulated response of the representative model for each cluster. If the simulated response of the representative model farthest from the history data be m, and the simulated response of the interested variable be RF^m, the deviation of the simulated response from the history data can be

written in Eq. (2.19) given an history data RF_{ref}.

$$\sigma_m^2 = \left| RF_{ref} - RF^m \right|^2 \tag{2.19}$$

Assuming a Gaussian distribution for the difference between simulated and history values ($N(RF_{ref}, \sigma_m^2)$), probability envelopes around the history data can be computed. Then, the likelihood function, $P(RF_{ref} \left| z^m(u) \right.)$ can be calculated according to the position of the simulated response within the probability envelope. The maximum likelihood function is selected among likelihood functions at every time step because the simulated response may not follow any one of the calculated probability contours. This is demonstrated in **Figure 2.11** and the likelihood function in this example is 0.66.
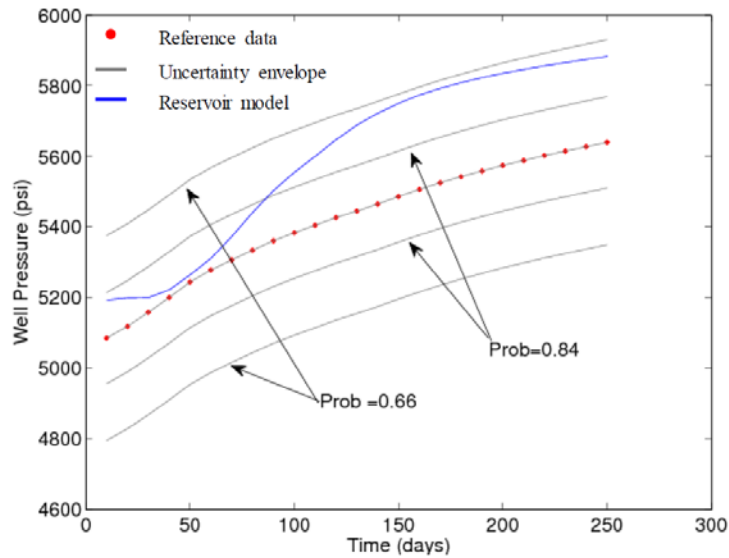

Figure 2.11 Uncertainty envelopes around reference data. The production data of one reservoir model falls within the 66% probability envelope (Mantilla, 2010).

3) Calculating posterior probability of each cluster

Using Bayes' rule, the posterior probability of each cluster can be computed shown as Eq. (2.20), knowing the likelihood function. Here, the numerator in Eq. (2.20) is the likelihood function and the denominator in Eq. (2.20) is the prior probability of the response RF_{ref} and can be calculated from the law of total probability as seen in Eq. (2.21).

$$P(z^m(u)|RF_{ref}) = \frac{P\left(RF_{ref}|z^m(u)\right)}{P(RE_{ref})} \times P(z^m(u)) \qquad (2.20)$$

$$P(RF_{ref}) = \sum_{m=1}^{k} P\left(RF_{ref}|z^m(u)\right) \cdot P(z^m(u)) \qquad (2.21)$$

4) Stopping criterion

The model selection algorithm is an iterative process, where the clustering and Bayesian updating is repeated using the best-fit models from the previous iteration. Therefore, a criterion is required to stop iterations. At any stage in the process, if the posterior probability of clusters are same or the number of models remaining in the cluster is below certain number, the model selection algorithm is stopped.

3. Reservoir characterization with FMM and model selection

Figure 3.1 summarizes the conventional method, which groups reservoir models based on static properties without forward modeling, such as fracture half-lengths and mean permeability, and performs model selection. The conventional method cannot consider dynamic connectivity of reservoir because it uses static properties to cluster reservoir models. In this thesis, SRV which can reflect dynamic connectivity of a reservoir is suggested in order to overcome the problem. **Figure 3.2** illustrates the procedures for the proposed method.

The first step of the proposed method is to generate 400 reservoir models via Sequential Gaussian Simulation (SGS) using static data and to add fracture half-lengths, fracture permeability and enhanced region to the models. The initial models should be wide so that the models represents the uncertainty in fracture properties and heterogeneity. **Table 3.1** is parameters and the associated uncertainties used to generate initial models. The fracture parameters follow a uniform distribution. **Figure 3.3** shows examples of reservoir models and gives an idea about the variety of fracture geometries used.

Then, run 400 models through FMM to get SRV in order to group 400 models according to their similarities. In this research, Hausdorff distance of SRV is defined as a connectivity measure. This motivation comes from the fact that reservoir models with similar SRV distribution share similar production data. Conversely, it is expected that reservoir models with dissimilar SRV distribution exhibit dissimilar production data. Based on the above assumption, the production data of the representative model of each cluster is a good representation of the production data from all the reservoir models of that cluster.

K-means clustering is performed to make clusters and select the representative models. The deviation of the simulated production data of the representative models from the observed production data is used to compute the posterior probability for selecting a cluster. A Bayesian scheme is presented for accomplishing this. A cluster is sampled on the basis of the posterior probability and the process is stopped when the number of reservoir models in the final cluster is less than fifteen. The last step of the proposed method is to predict estimated ultimate recovery (EUR) with the final set of models.
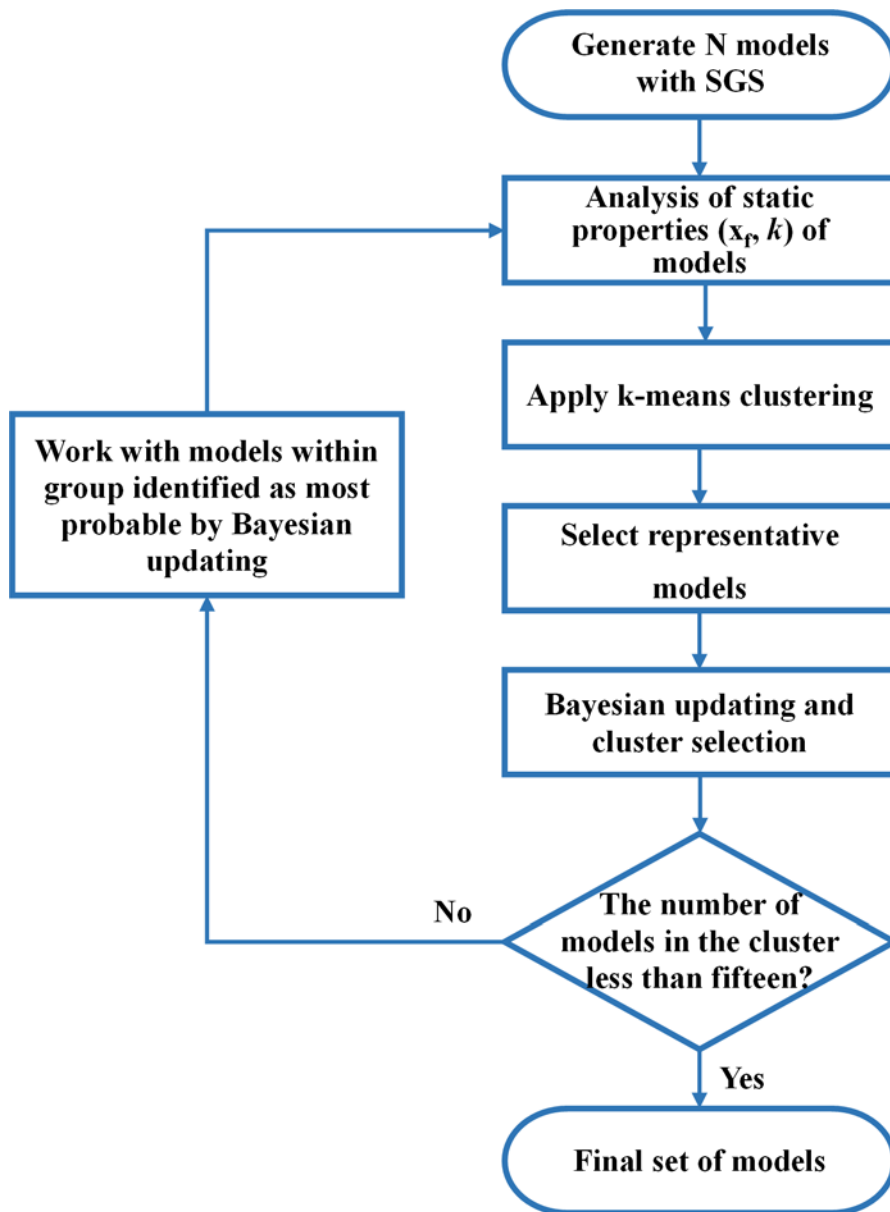
Figure 3.1 Flow chart of the conventional method.
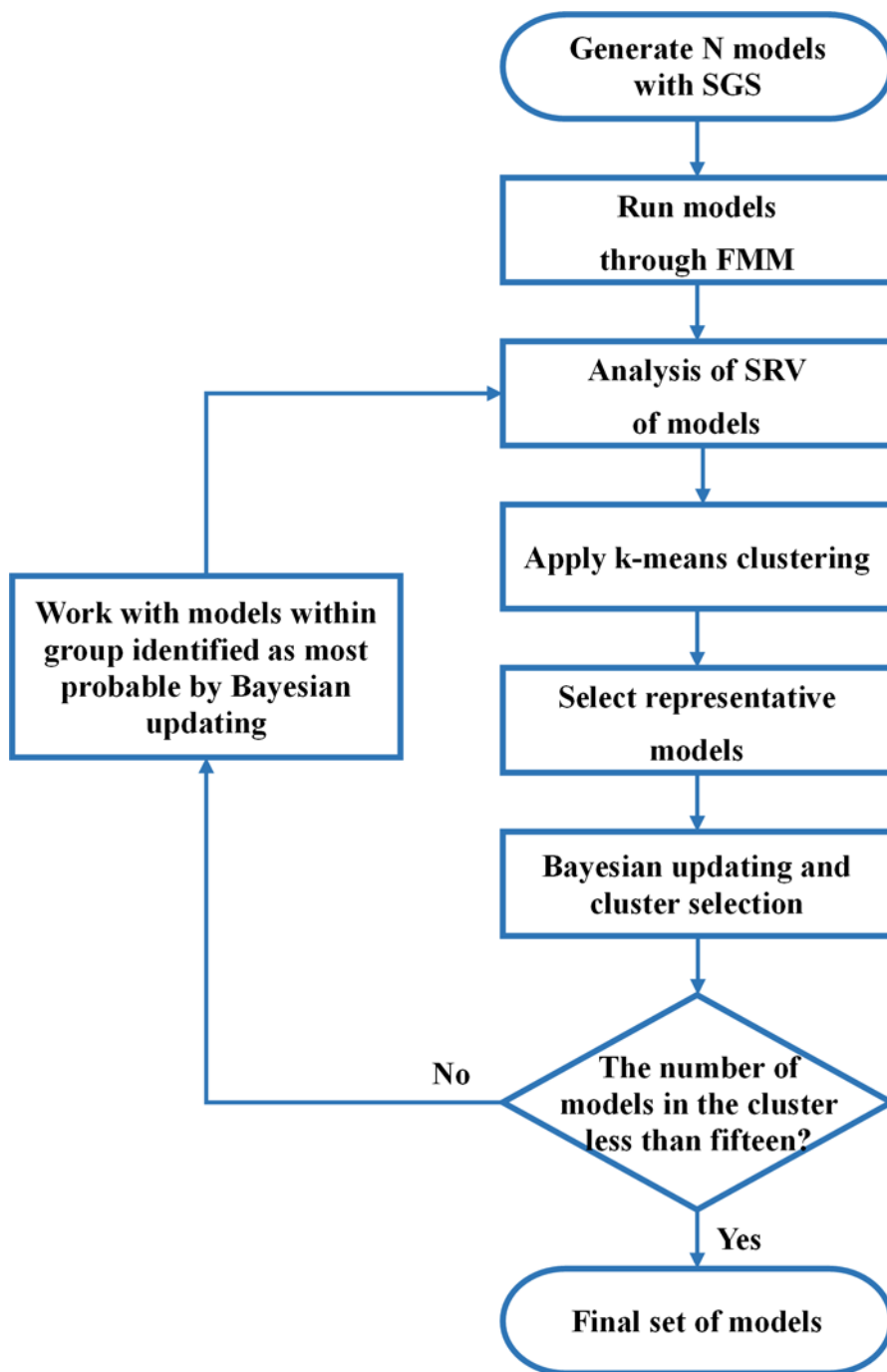
Figure 3.2 Flow chart of the proposed method.

Table 3.1 Distribution and the ranges of parameters

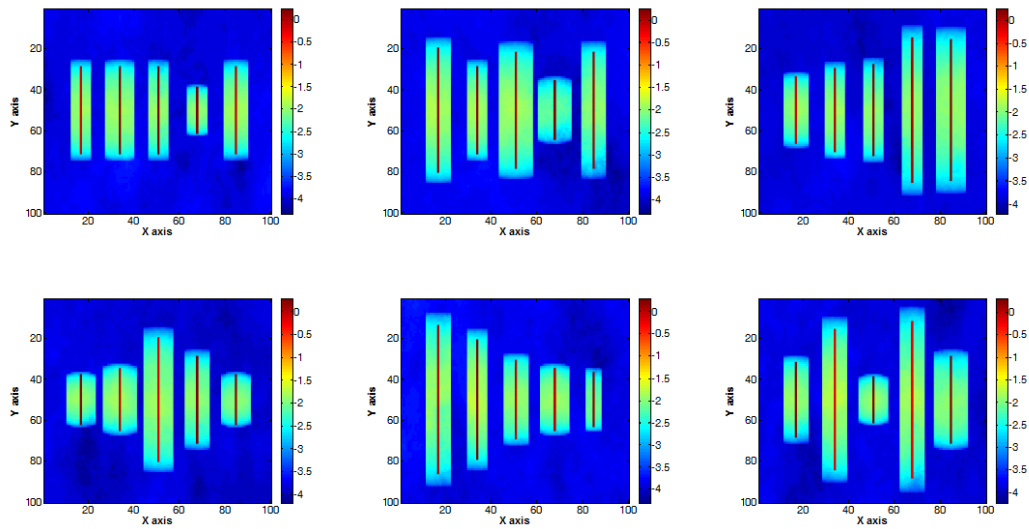| Parameters	Distribution	Min / max
Hydraulic fracture half-length, ft	uniform	150 / 800
Hydraulic fracture permeability, md	uniform	0.5 / 2.0
Enhanced region (x-direction), ft	uniform	60 / 140

Figure 3.3 Examples of generated reservoir models. The horizontal well is located from the left to the right.

4. Results

4.1 Reference field

The reference field, as show in **Figure 4.1**, is a 3-D square synthetic field of which the dimension is 2,000 ft × 2,000 ft × 100 ft. It consists of $100 \times 100 \times 5$ cells, total 50,000 cells. **Figure 4.2** is log permeability distribution of the reference field generated by SGeMS (Standford Geostatistical Modeling Software). The average of matrix permeability is 1.3E-4 md and the range is 2.2E-4 – 4.89E-5 md. Porosity is all the same as 0.07. Initial reservoir pressure is 1,500 psi and reservoir and fluid properties are given in **Table 4.1**. There are one horizontal well with 5 fractures and it has constant bottomhole pressure condition of 500 psi.

Figure 4.3 shows SRV and fracture patterns which are classified in three categories: connected SRV, isolated SRV and two-wings fractures without SRV. In this thesis, isolated SRV is assumed. The enhanced permeability within SRV due to hydraulic fracturing has to be assumed. In this thesis, a linear permeability gradient is assumed to include the change of permeability of enhanced region as a function of distance from the well. Therefore, the enhanced permeability is equal to the matrix permeability where it is far from the well. Similarly, the enhanced permeability is introduced with a permeability enhancement of 50 times that of matrix permeability where it is close to the well. The fracture permeability is from 0.5 md to 2 md and randomly distributed.

Figure 4.4 is cumulative gas production rate of the reference field from a numerical simulator, CMG GEM.
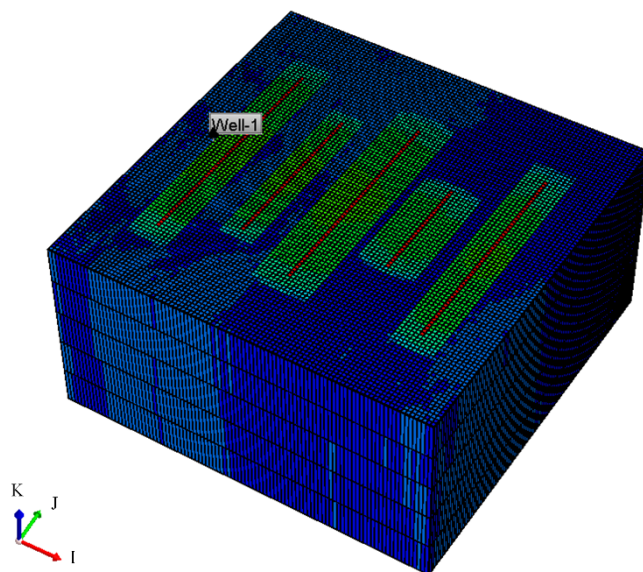
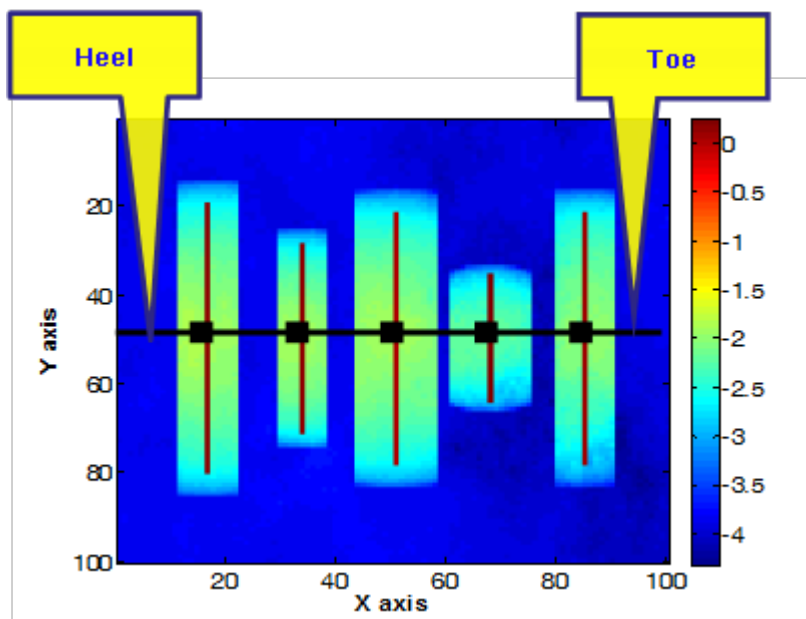Figure 4.1 3D view of the reference field**.**

Figure 4.2 Log permeability distribution and horizontal well location of the reference

field.

Table 4.1 Reservoir and fluid data of the reference field

| Reservoir properties	Value
Reservoir grid, X×Y×Z	100×100×5
Δx=Δy=Δz, ft	20
Initial reservoir pressure, psia	1,500
Temperature, °F	100
Bottom hole pressure, psia	500
Reservoir depth, ft	3,380
Matrix permeability range, md	2.2E-4 – 4.89E-5
Matrix porosity, fraction	0.07
Rock density, lbm/ft3	120
Langmuir volume, scf/ton	167
Hydraulic fracture half-length, ft	600, 420, 560, 280, 560
Hydraulic fracture height, ft	100
Hydraulic fracture permeability, md	1.4, 1.4, 0.9, 1.8, 1.1
Enhanced region (x-direction), ft	100, 80, 140, 140, 100
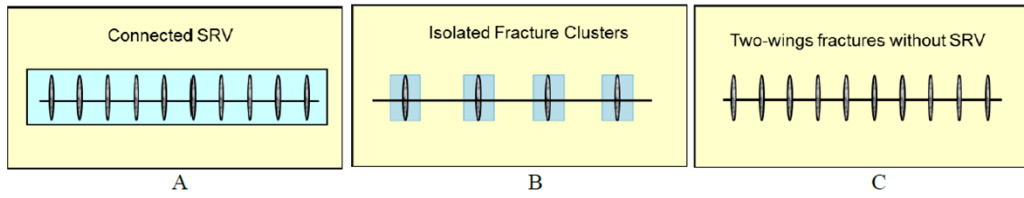
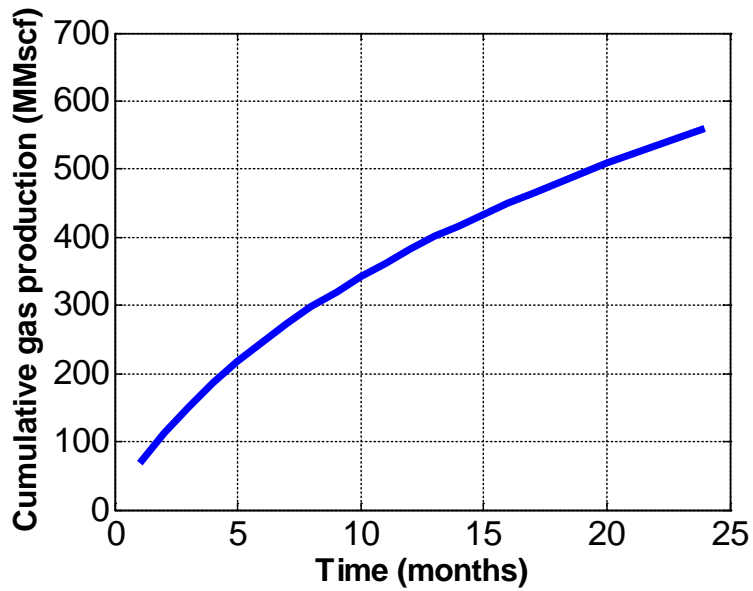Figure 4.3 Possible SRV/Fracture patterns (Chu et al., 2012).

Figure 4.4 Cumulative gas production from the reference field**.**
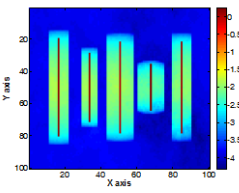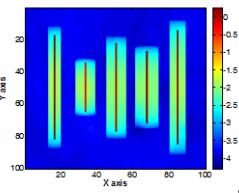
4.2 SRV calculation using FMM
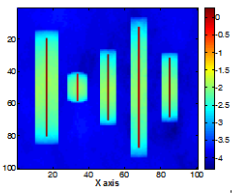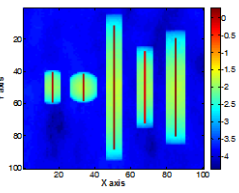
All members of the initial model set were analyzed using FMM. For the purpose of discriminating between models, SRV are calculated and the locations of SRV are recorded to compute Hausdorff distance.

Table 4.2 represents the similarity of reservoir models according to Hausdorff distance. The reservoir model having small Hausdorff distance is similar to the reference field, and the reservoir model having large Hausdorff distance is far from the reference field.

Figure 4.5 is the result of applying MDS after computing Hausdorff distance of SRV for 400 reservoir models. The models are projected onto the 2D MDS plane. The characteristics of the plane is as below.

1) Left side: reservoir having big SRV

2) Right side: reservoir having small SRV

3) Upper side: reservoir having long SRV to the toe part

4) Lower side: reservoir having long SRV to the heel part

Table 4.2 Calculation of the Hausdorff distance (1st column: reference realization, H in the 2nd-4th columns: the Hausdorff distance between the reference and itself)

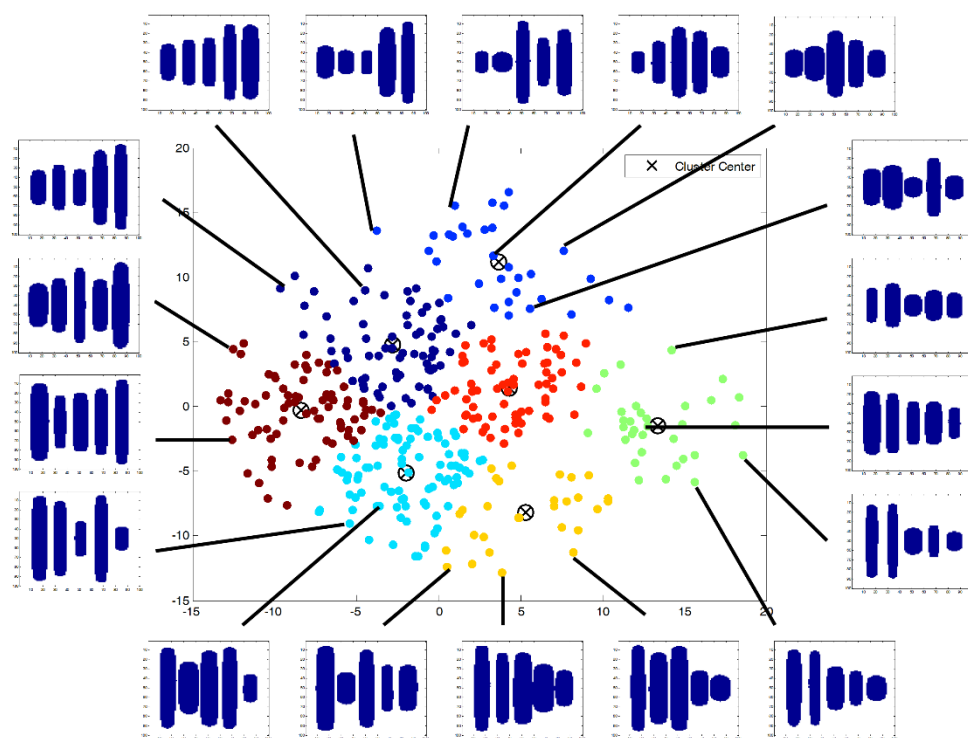| Permeability distribution	Distance to the reference image Small − − − − − − − −> Large		
Reference	H = 8.25	H = 16.97	H = 24.00

Figure 4.5 MDS result in 2D.

4.3 Application of model selection approach

Figure 4.6 is the effectiveness of clustering (η_k) computed for different number of clusters for the projected models. The analysis shows that the optimum number of clusters in this case is 7 where the value is almost constant. Hence, the models are divided into 7 clusters and representative models are picked for each cluster. The representative models are run through a numerical simulator (CMG-GEM) and the cumulative gas production rate of the reference field is used to compute the likelihood function for the Bayesian calculation discussed in Section 2.3.

Table 4.3 is the result of first iteration of model selection. The posterior probability of the representative model in cluster 4 is 0.3800, the highest value among the clusters. Following cluster 4, cluster 2 is the second highest probability with 0.2115. It is also found in **Figure 4.7** that the representative model of cluster 4 is closest to the history data, and the models in cluster 4 are chosen for the subsequent step. Cluster 5 with the lowest probability shows different production profile compared to the history data.

K-means clustering of the 65 models in cluster 4 gives seven clusters as the ideal cluster number, and simulated results of the representative models are compared to the history data (**Table 4.4** and **Figure 4.8**). The posterior probability of the representative model of cluster 7 is 0.4134, the highest value among clusters. Here, cluster 6 is the closest to the history data, but cluster 6 has only 3 models leading small posterior probability. Cluster 7 contains 11 models, which satisfies the stopping criterion, and cumulative gas production is predicted for 10 years with 11 models (**Figure 4.9**).

For verification of the proposed method, same procedure is performed to conventional method, only using static parameters for clustering. **Figure 4.10** is cumulative gas production up to 10 years with final models of the conventional method.

It shows different production profile.

Figure 4.11 is a boxplot of EUR at the 10th year. Each EUR is divided by the EUR of the reference field for regularization. Therefore, if the boxplot contains the value 1, we can say that the method captures the true EUR. The boundaries of the box are the first quartile (Q_1) and the third quartile (Q_3) and the red line is the median (Q_2). Dotted lines from the box are the maximum and minimum value within a 1.5 times of inter-quartile range (IQR) (Choi, 2013). Conventional method reduces the range of uncertainty, but shows biased uncertainty without including true EUR value within IQR. On the other hand, proposed method shows reliable EUR result, overcoming the limitation of the conventional method.

Figure 4.12 shows 4 models from the final retained cluster through conventional method and proposed method. Fracture distribution of reservoir models from conventional method differs from that of the reference field. On the other hand, fracture distribution of reservoir models from proposed method is consistent with the reference field due to successful clustering based on SRV.

The reason why proposed method yields reliable reservoir characterization results than conventional method comes from clustering. It is important to define a distance to project reservoir models having similar performance on the MDS plane locating close to each other. Conventional method rarely depicts production performance because the method defines static properties, such as permeability and fracture half-length, as a distance having no dynamic connectivity of reservoir. However, proposed method shows reliable production performance with successful clustering because the method defines SRV, regions within the fractures that affect production, as a distance.
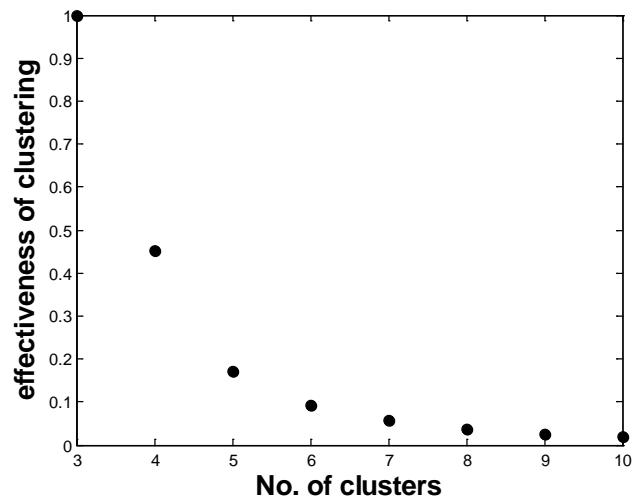
Figure 4.6 Plot of effectiveness of clustering versus number of clusters

for the reference field.

Table 4.3 Results of model selection, first iteration

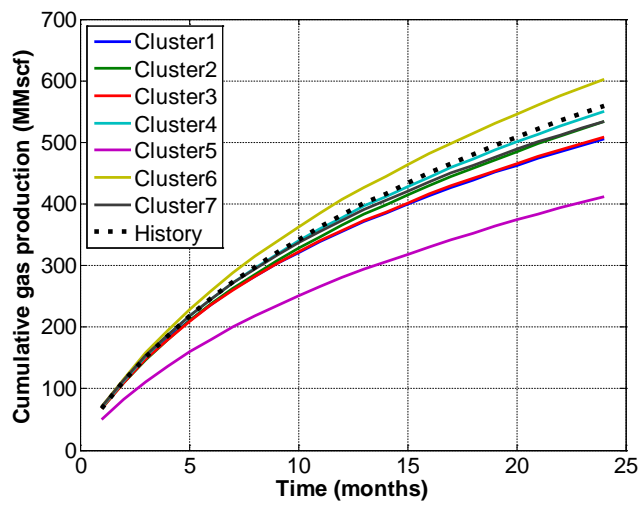| Cluster number	4	2	6	7	3	1	5	Total
# of models	65	61	77	38	64	63	32	400
Prob	0.3800	0.2115	0.1356	0.1353	0.0753	0.0624	6E-7	

Figure 4.7 Comparison of simulation results to actual field data, first iteration.

Table 4.4 Results of model selection, second iteration

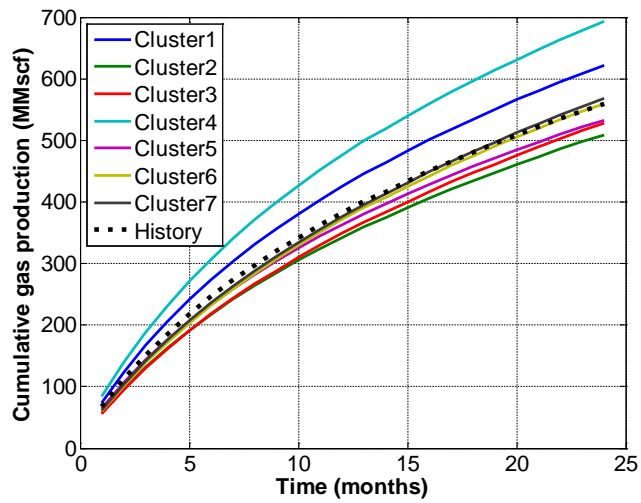| Cluster number	7	5	1	6	3	2	4	Total
# of models	11	6	13	3	13	5	14	65
Prob	0.4134	0.3633	0.1088	0.0464	0.0350	0.0331	0.0001	

Figure 4.8 Comparison of simulation results to actual field data, second iteration.
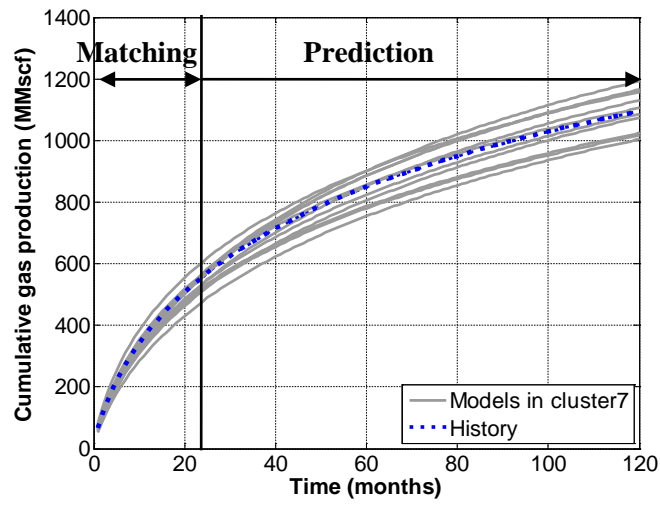
Figure 4.9 Cumulative gas production for 10 years by proposed method
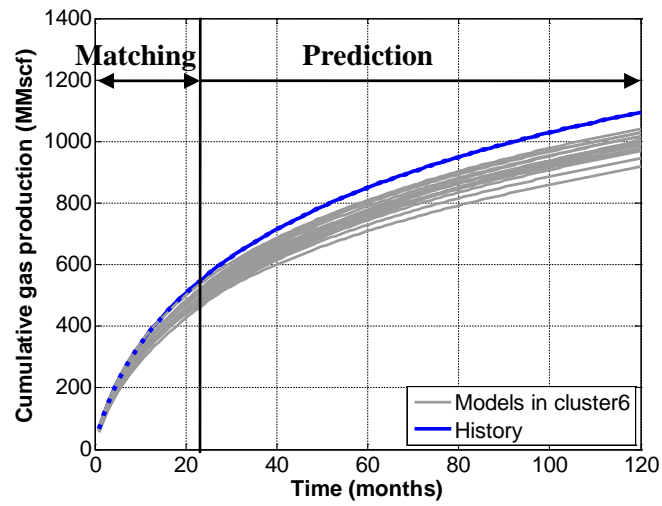
(selected models from the final cluster).

Figure 4.10 Cumulative gas production for 10 years by conventional method

(selected models from the final cluster).
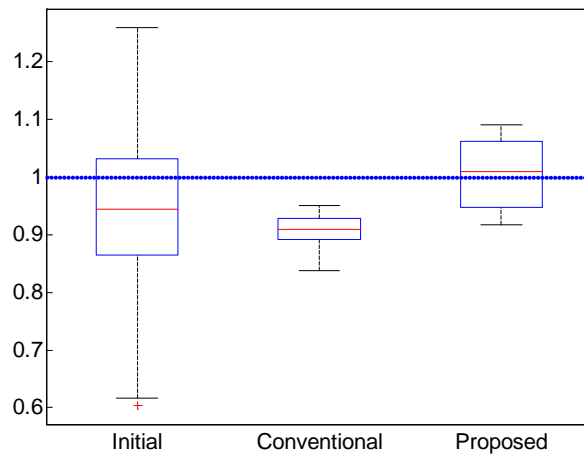
Figure 4.11 Uncertainty range of EUR at 10 years.

Model 1   Model 2

Model 3   Model 4

a) Conventional method

Reference model

Model 1   Model 2

Model 3   Model 4

b) Proposed method
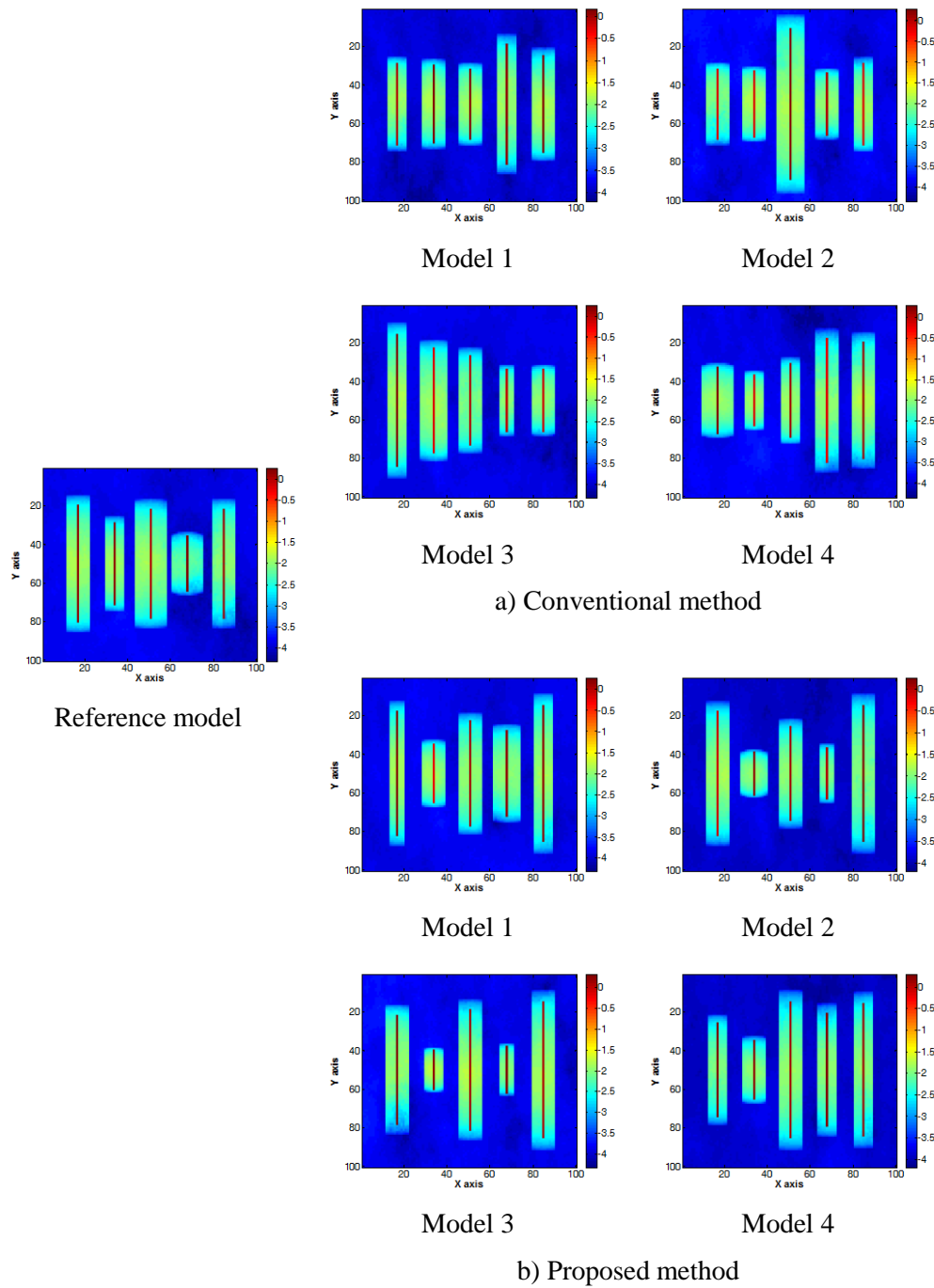
Figure 4.12 Log permeability of 4 representative models of conventional and proposed

method.

The result of EUR estimation on the number of cluster (3, 5, 7, 9, 11) from the proposed method is displayed in **Figure 4.13**. It shows that if the cluster number is less than 7, the result is either large uncertainty range or biased uncertainty without including true EUR value within IQR. Because it is difficult to encompass a range of initial reservoir models with only little clusters. However, if the cluster number is more than 7, the result shows reliable prediction including true value within IGR. To sum up, there is the optimum number of cluster in model selection process and it corresponds with the number from Bhowmik(2014)'s method. More results of the other reservoirs with different fracture geometries are presented in Appendix.
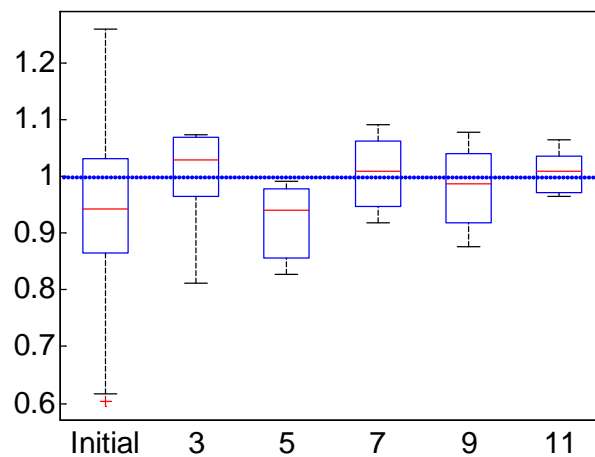

Figure 4.13 Uncertainty range of EUR at 10 years.

Another reservoir model with uniform fracture distribution is generated to verify the proposed method (**Figure 4.14**). The average of matrix permeability is 1.2E-4 md and the range is 2.1E-4 – 4.5E-5 md. **Table 4.5** represents fracture properties, such as fracture half-length, fracture permeability and enhanced region.

Figure 4.15 is the effectiveness of clustering (η_k) computed for different number of clusters for the projected models. The analysis shows that the optimum number of clusters in this case is 7 where the value is almost constant. Hence, the models are divided into 7 clusters and representative models are picked for each cluster.

Table 4.6 and **Figure 4.16** are the results of first iteration of model selection. It was found that the representative model in cluster 7 is closest to the history data, and it is chosen for the subsequent step. K-means clustering of the 69 models in cluster 7 gives seven clusters as the ideal number of clusters, and simulated results of the representative models are compared to the history data (**Table 4.7** and **Figure 4.17**). The posterior probability of the representative model in cluster 1 is 0.5695, the highest value in the clusters. Here, cluster 6 is the closest to the history data, but the number of models in the 6 cluster is lower than cluster 1 leading small posterior probability. Cluster 1 contains 14 models, which satisfies the stopping criterion, and cumulative gas production is predicted with 14 models for 10 years (**Figure 4.18**). It shows that proposed method represent similar production profile with the history data.

Figure 4.19 is cumulative gas production up to 10 years with final models of the conventional method. It shows different production profile compared to the history data. **Figure 4.20** is a boxplot of EUR at the 10th year. Each EUR is divided by the EUR of the reference field for regularization. Conventional method reduces the range of uncertainty, but shows biased uncertainty without including true EUR value within IQR. On the other hand, proposed method shows reliable EUR result, overcoming the

limitation of the conventional method.

Figure 4.21 shows 4 models from the final retained cluster through conventional method and proposed method. Fracture distribution of reservoir models from conventional method differs from that of the reference field. On the other hand, fracture distribution of reservoir models from proposed method is consistent with the reference field due to successful clustering based on SRV.
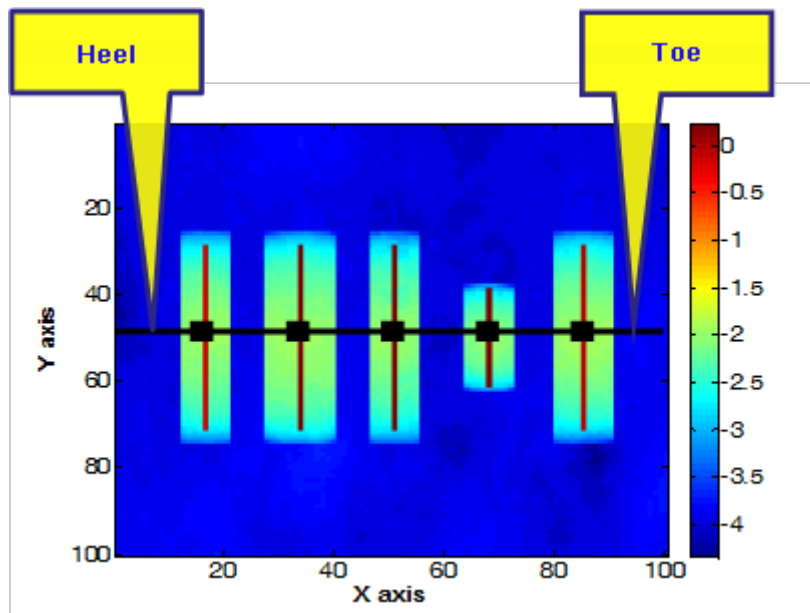
Figure 4.14 Log permeability distribution and horizontal well location of the reference field (uniform fractures)

Table 4.5 Reservoir data of the reference field (uniform fractures)

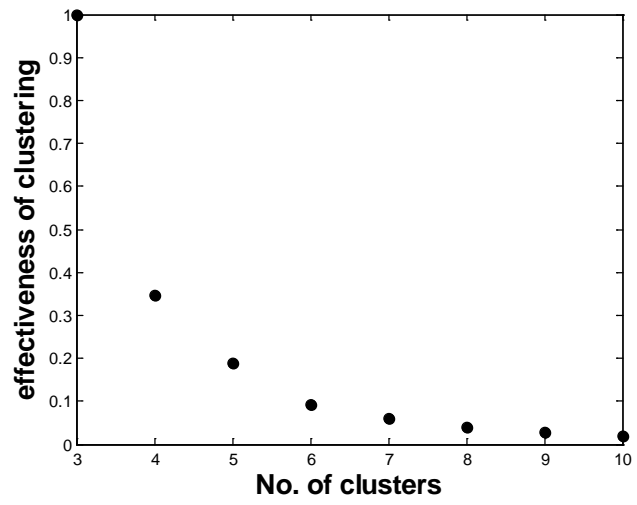| Reservoir properties	Value
Hydraulic fracture half-length, ft	420, 420, 420, 220, 420
Hydraulic fracture permeability, md	0.7, 1.6, 1.7, 1.7, 0.8
Enhanced region (x-direction), ft	80, 120, 80, 80, 100

Figure 4.15 Plot of effectiveness of clustering versus number of clusters

for the reference field (uniform fractures).

Table 4.6 Results of model selection, first iteration (uniform fractures)

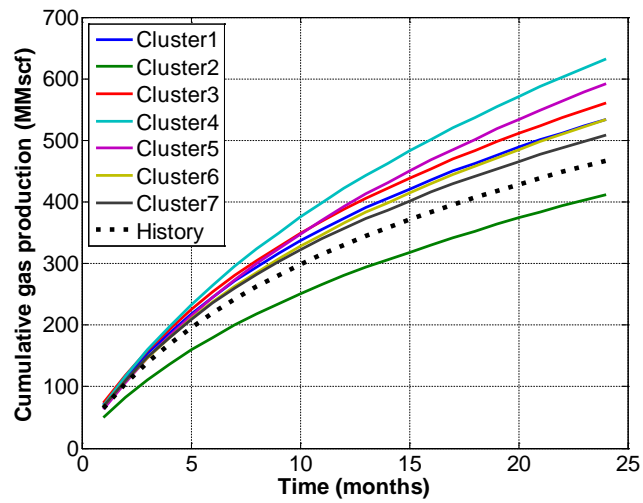| Cluster number	7	6	1	3	5	4	2	Total
# of models	69	60	40	67	52	80	32	400
Prob	0.5479	0.2731	0.1083	0.0492	0.0188	0.0027	5E-5	

Figure 4.16 Comparison of simulation results to actual field data, first iteration

(uniform fractures).

Table 4.7 Results of model selection, second iteration (uniform fractures)

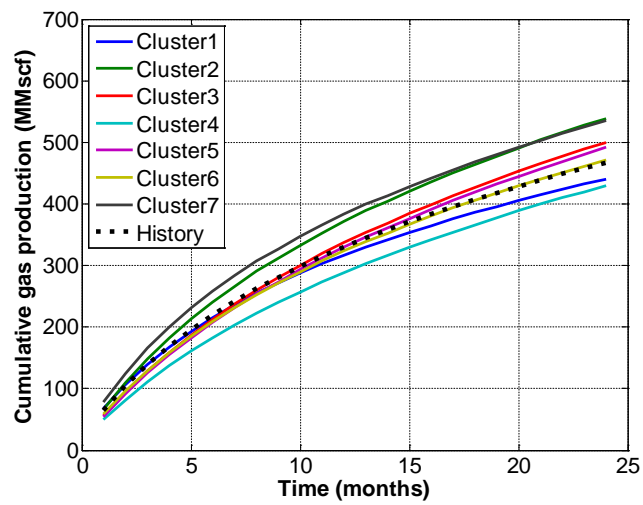| Cluster number	**1**	6	3	5	2	4	7	Total
# of models	**14**	8	11	8	8	11	9	69
Prob	**0.5695**	0.2504	0.1153	0.0572	0.0030	0.0028	0.0018	

Figure 4.17 Comparison of simulation results to actual field data, second iteration
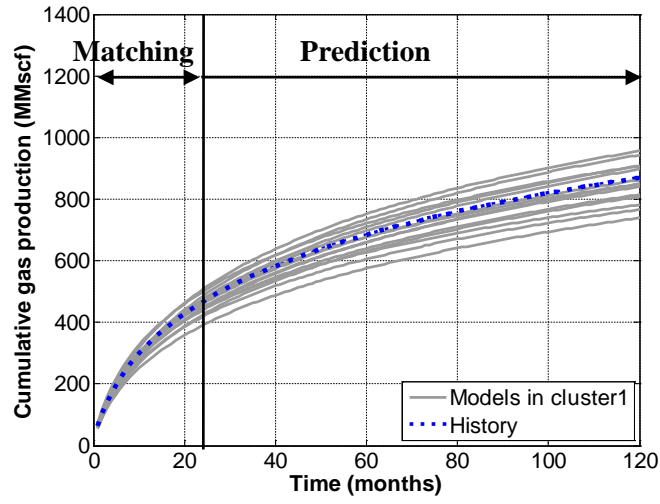
(uniform fractures).

Figure 4.18 Cumulative gas production for 10 years by proposed method
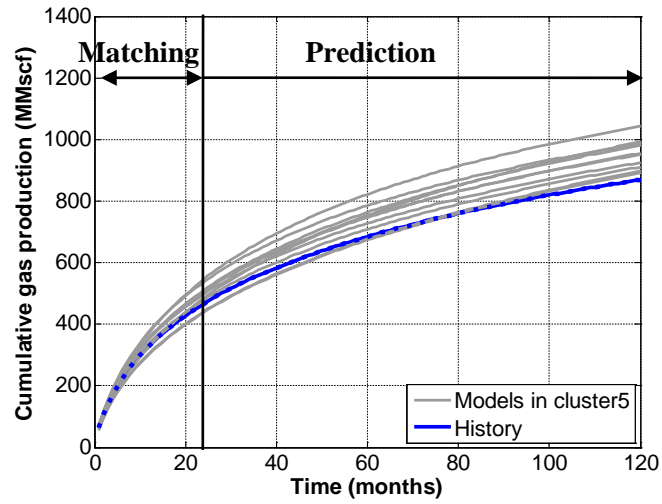
(uniform fractures).

Figure 4.19 Cumulative gas production for 10 years by conventional method
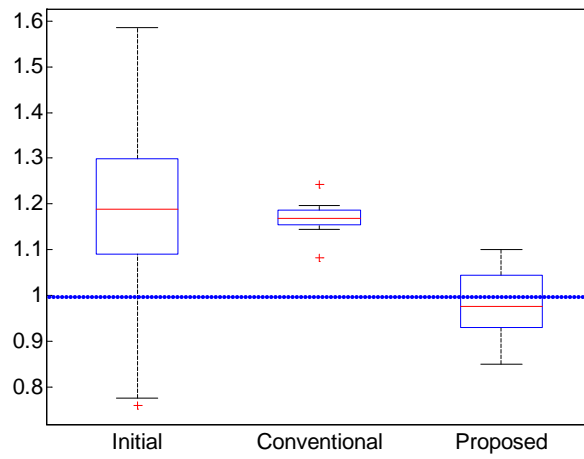
(uniform fractures).

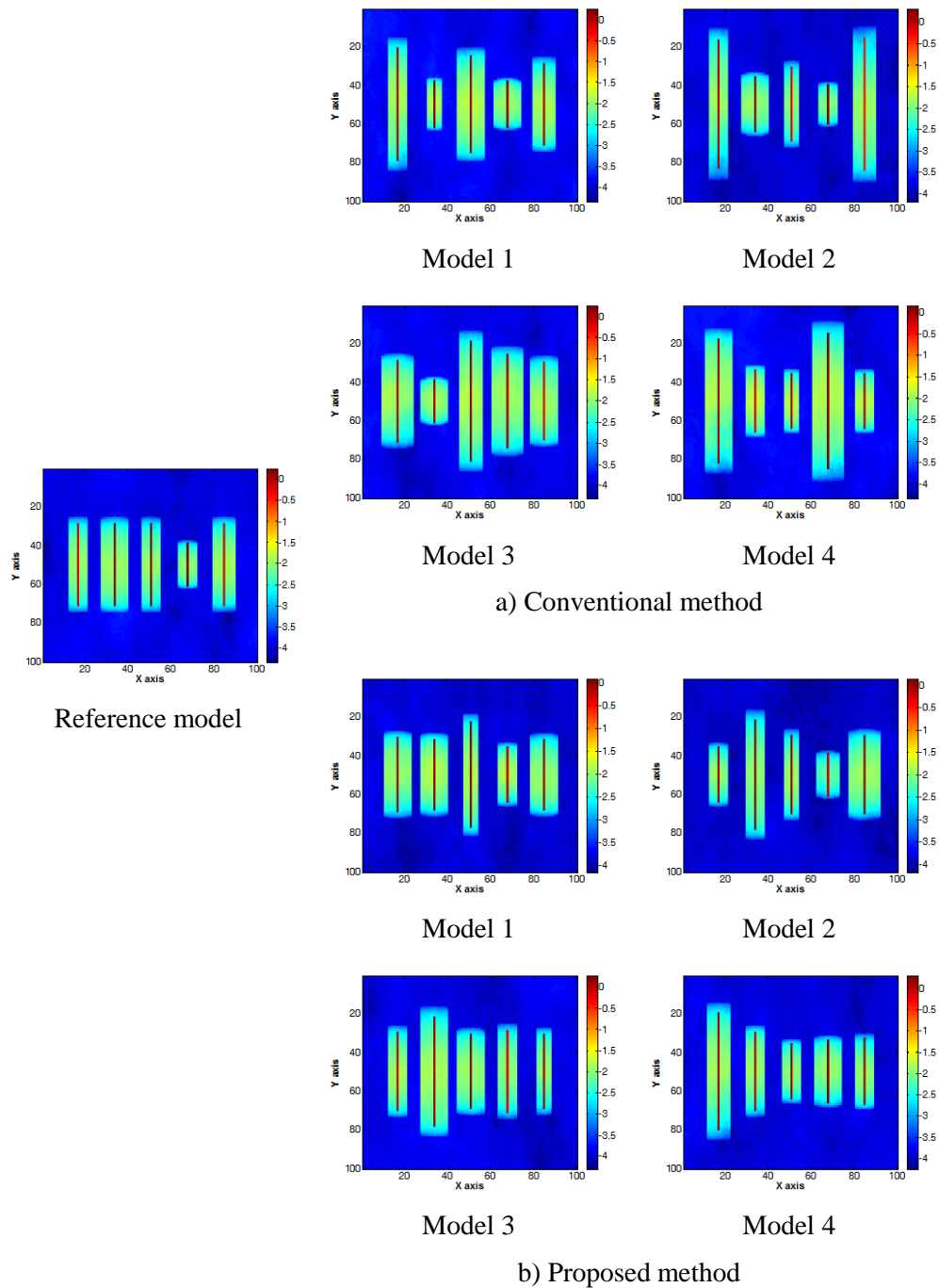Figure 4.20 Uncertainty range of EUR at 10 years (uniform fractures).

Model 1   Model 2

Model 3   Model 4

Reference model

a) Conventional method

Model 1   Model 2

Model 3   Model 4

b) Proposed method

Figure 4.21 Log permeability of 4 representative models of conventional and proposed method (uniform fractures).

Figure 4.22 is the analysis of EUR estimation on the number of cluster (3, 5, 7, 9, 11). It shows that if the number of cluster is less than 7, the result has biased uncertainty without including true EUR value within IQR. The results correspond to the results of the previous reservoir model.
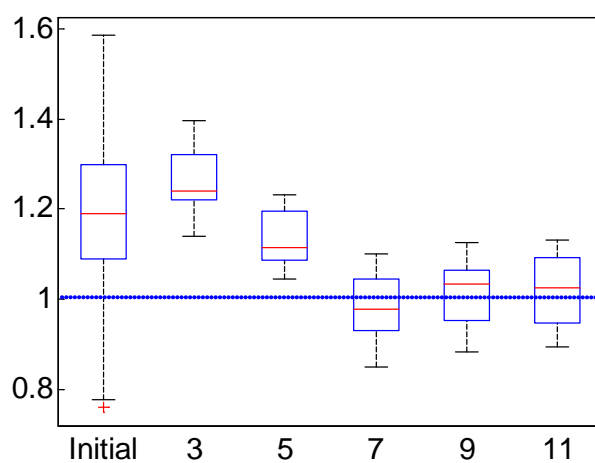

Figure 4.22 Uncertainty range of EUR at 10 years (uniform fractures).

5. Conclusion

In this thesis, a method is proposed to perform shale gas reservoir characterization and production forecasts using FMM combined with model selection approach. SRV acquired from FMM is utilized to reflect dynamic connectivity of reservoir for clustering procedure and model selection for selecting a cluster close to the history data is performed. The proposed method is applied to various shale gas reservoirs with different fracture geometries. The conclusions of this research work are organized as below.

1. The conventional method using static properties for clustering procedure gives improper results sharing different characteristics among each cluster because it cannot reflect the dynamic connectivity of reservoir. However, the proposed method is possible to group models with similar SRV and fracture distributions.

2. The results of conventional and proposed method are compared to verify future production of shale gas reservoir. As a result, the proposed method reduces the uncertainty range of EUR compared to initial reservoir models and contains true EUR within IQR compared to the conventional method showing biased uncertainty regardless of fracture geometries.

3. The proposed method yields a cluster of models that share the reservoir characteristics, rather than a single best-fit model. The models in the cluster can be used for uncertainty assessment of future production.

The proposed method shows more reliable EUR prediction than the conventional method. Furthermore, the method has no disadvantage over the conventional method because FMM can evaluate quickly and efficiently the SRV of shale gas reservoirs. The proposed method is expected not only to establish development strategies but also to make a decision for shale gas plays with the probability distribution of production forecasts.

Reference

Bhowmik, S., Srinivasan, S., and Bryant, S. L. : "Predicting the Migration of CO_2 Plume Using Injection Data and a Distance-Metric Approach to Reservoir-Model Selection," SPE paper 139709 presented at the SPE International Conference on CO_2 Capture, Storage, and Utilization, New Orleans, Louisiana, 10–12 November 2010.

Bhowmik, S. 2014. Particle Tracking Proxies for Prediction of CO_2 Plume Migration Within a Model Selection Framework. PhD Dissertation, The University of Texas at Austin, Austin, Texas (May 2014).

Caers, J. 2011. *Modeling Uncertainty in the Earth Sciences*. Chichester, UK: John Wiley & Sons Ltd.

Chu, L., Ye, P., Harmawan, I., Du, L., and Shepart, L. : "Characterizing and Simulating the Non-Stationariness and Non-Linearity in Unconventional Oil Reservoirs: Bakken Application," SPE paper 161137 presented at the SPE Canadian Unconventional Resources Conference, Calgary, Alberta, Canada, 30 October–1 November 2012.

Choi, Y. 2014. *Multi-dimensional Scaling*, Paju, Korea: Free Academy.

David, S. 2013. US to begin exporting 'fracked' gas. BBC News, 16 July 2013, http://www.bbc.co.uk/news/science-environment-23317370 (accessed 14 July 2014)

Dong, Z., Hoditch, S.A., McVay, D.A., Ayers, W.B., Lee, J., and Morales, E. : "Probabilistic Assessment of World Recoverable Shale Gas Resources," SPE paper 167768 presented at the SPE/EAGE European Unconventional Conference and Exhibition, Vienna, Austria, 25-27 February 2014.

Dubuisson, M.-P. and Jain, A. K. 1994. A Modified Hausdorff Distance for Object Matching. *ICPR* **94** (1): 566-568.

Holditch, S. A. 2010. Shale Gas Holds Global Opportunities. *The American Oil & Gas Reporter*, August 2010 Editor's Choice.

Jin, J. 2011. Oil Production Analysis in Oil Sands Reservoirs Using distance Based Clustering. MS Thesis, Seoul National University, Seoul, South Korea.

Kim, J. U., Datta-Gupta, A., Brouwer, R. and Haynes, B. Jr. : "Calibration of High-Resolution Reservoir Models Using Transient Pressure Data," SPE paper 124834 presented at the 2009 SPE Annual Technical Conference and Exhibition, New Orleans, Louisiana, USA, 4-7 October 2009.

Lee, K. 2014. Channelized Reservoir Characterization using Ensemble Smoother with a distance-Based Method. PhD Dissertation, Seoul National University, Seoul, Korea (August 2014).

Mantilla, C. A. 2010. Feedback Control of Polymer Flooding Process Considering Geologic Uncertainty. PhD Dissertation, The University of Texas at Austin, Austin, Texas (December 2010).

Park, G. 2000. *Multi-dimensional Scaling*, Seoul, Korea: Kyoyookbook.

Park, J. 2014. Uncertainty Quantification of Reservoir Performances Using Streamline Based Inversion and Distance Based Method. MS thesis, Seoul National University, Seoul, Korea (February 2014).

Scheidt, C. and Caers, J. 2009. Representing Spatial Uncertainty Using Distances and Kernels. *Mathematical Geosciences* **41** (4): 397-419.

Sethian, J.A. 1996. *Level Set Methods and Fast Marching Methods*, New York, USA: Cambridge University Press.

Sethian, J.A. and Vladmirsky, A. 2000, Fast Methods for the Eikonal and Related Hamilton-Jacobi Equations on Unstructured Meshes. *Proceedings of the National Academy of Sciences* **97** (11): 5699-5703.

Singh, H. and Srinivasan, S. : "Uncertainty Analysis by Model Selection Technique and Its Application in Economic Valuation of a Large Field," SPE paper 164623 presented at the North Africa Technical Conference & Exhibition, Cairo, Egypt, 15–17

April 2013.

Suzuki, S. and Caers, J. 2008. A distance-based prior model parameterization for constraining solutions of spatial inverse problems. *Mathematical Geosciences* **40** (4): 445-469.

Vasco, D.W., Keers, and H., Karasaki, K. 2000. Estimation of Reservoir Properties Using Transient Pressure Data: An Asymptotic Approach. *Water Resoir. Res.* **36**: 3447-3465.

Xie, J., Yang, C., Gupta, N., King, M. J., and Datta-Gupta, A. : "Integration of Shale Gas Production Data and Microseismic for Fracture and Reservoir Properties Using Fast Marching Method," SPE paper 161357 presented at the SPE Eastern Regional Meeting, Lexington, Kentucky, USA, 3-5 October 2012.

Yin, J., Xie, J., Datta-Gupta, A., and Hill, A. D. : "Improved Characterization and Performance Assessment of Shale Gas Wells by Integrating Stimulated Reservoir Volume and Production Data," SPE Paper 148969 presented at the SPE Eastern Region Meeting, Columbus, Ohio, 17-19 August 2011.

Zhang, Z. and Fassihi, M. R. : "Uncertainty Analysis and Assisted History Matching Workflow in Shale Oil Reservoirs," SPE paper 168795 presented at the Unconventional Resources Technology Conference, Denver, Colorado, USA, 12–14 August 2013.

# Appendix A. Results of the proposed method

Appendix summarizes the results of the proposed method for shale gas reservoirs with different fracture geometry. The list of the results is as follows.
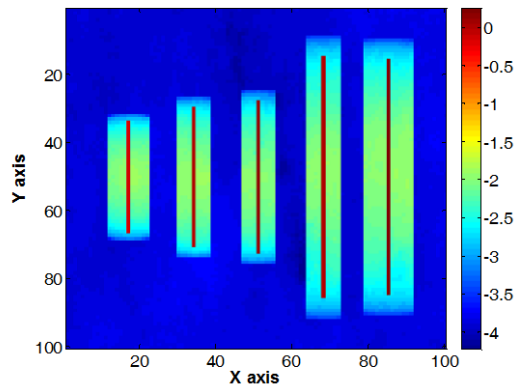
List of the results

- Permeability distribution of reference fields (Case1, Case2, Case3)

- Posterior probability

- Cumulative gas production for each cluster

- EUR prediction with the models in the final cluster
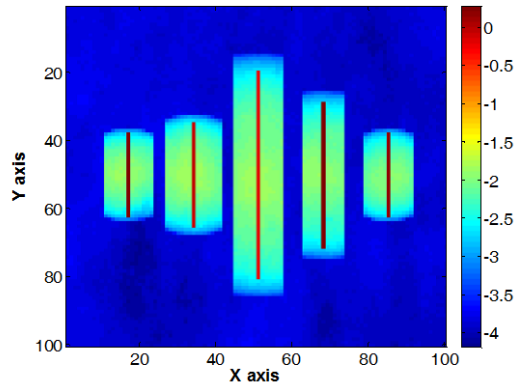
a) case 1
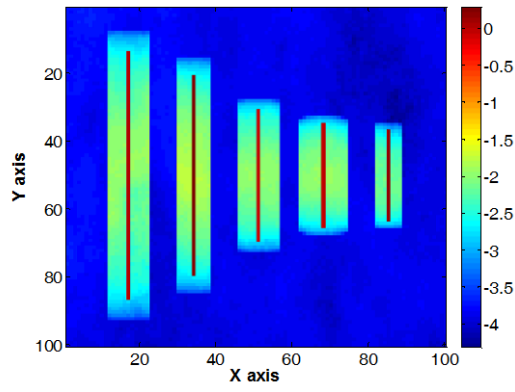
b) case 2

c) case 3

Figure A.1 Log permeability of reference fields: a) case 1, b) case 2, and c) case 3.

Model selection by proposed method with case 1

Table A.1 Results of model selection, first iteration by proposed method with case 1

Cluster number	**2**	6	5	1	7	4	3	Total
# of models	**41**	66	31	91	34	63	74	400
Prob	**0.5694**	0.3219	0.0793	0.0110	0.0105	0.0076	0.0003	
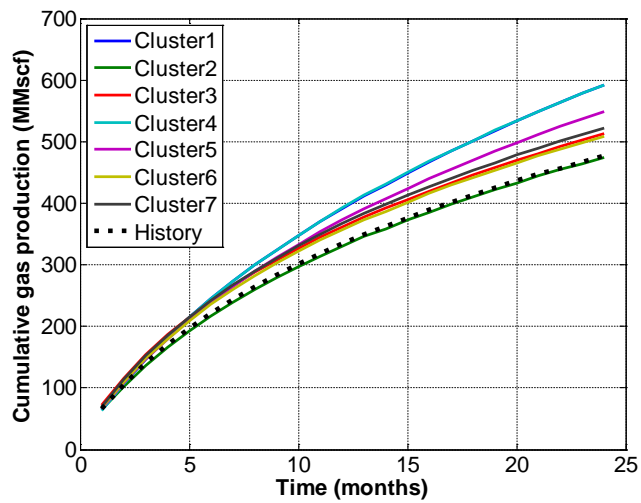
Figure A.2 Comparison of simulation results to actual field data, first iteration by proposed method with case 1.

Table A.2 Results of model selection, second iteration by proposed method with case 1

Cluster number	**7**	1	5	3	2	4	6	Total
# of models	**6**	4	5	10	3	10	3	41
Prob	**0.5838**	0.2858	0.0547	0.0377	0.0268	0.0069	0.0043	
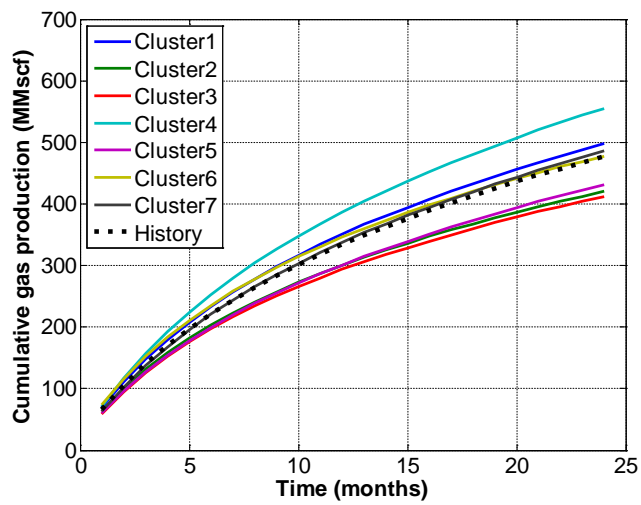
Figure A.3 Comparison of simulation results to actual field data, second iteration

by proposed method with case 1.
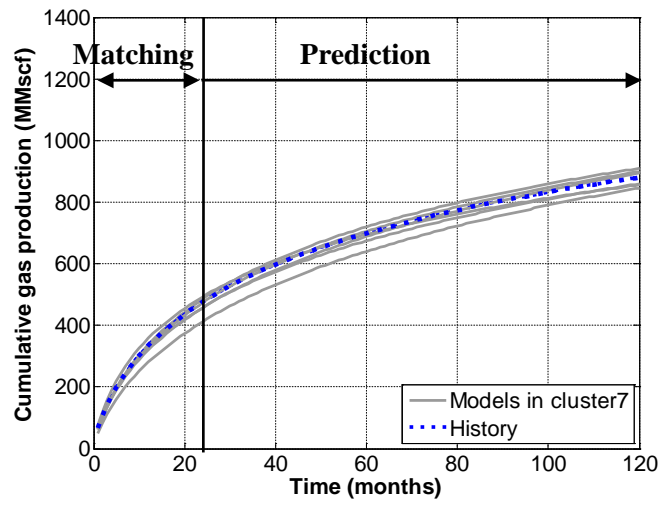
Figure A.4 Cumulative gas production for 10 years by proposed method with case 1.
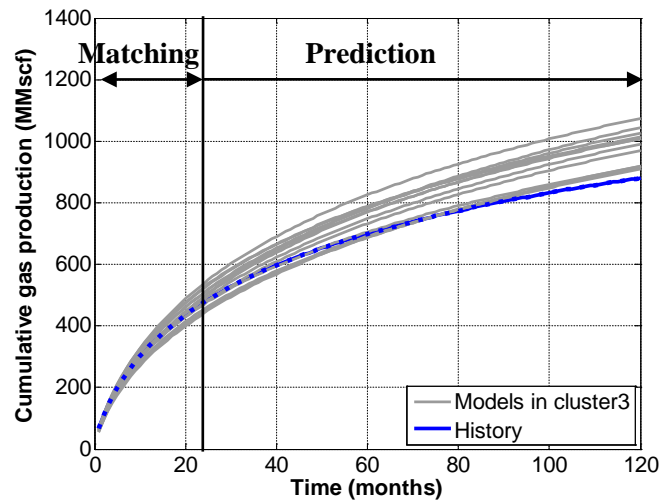
Figure A.5 Cumulative gas production for 10 years by conventional method with case 1.
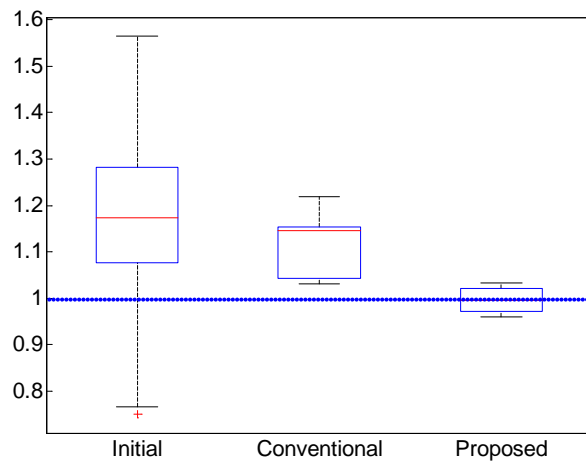
Figure A.6 Uncertainty range of EUR at 10 years with case 1.
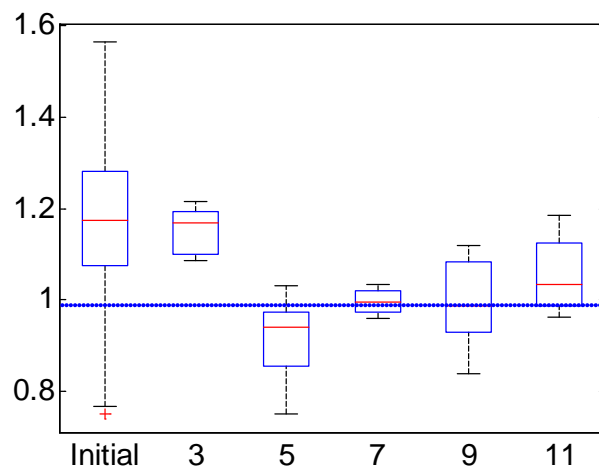
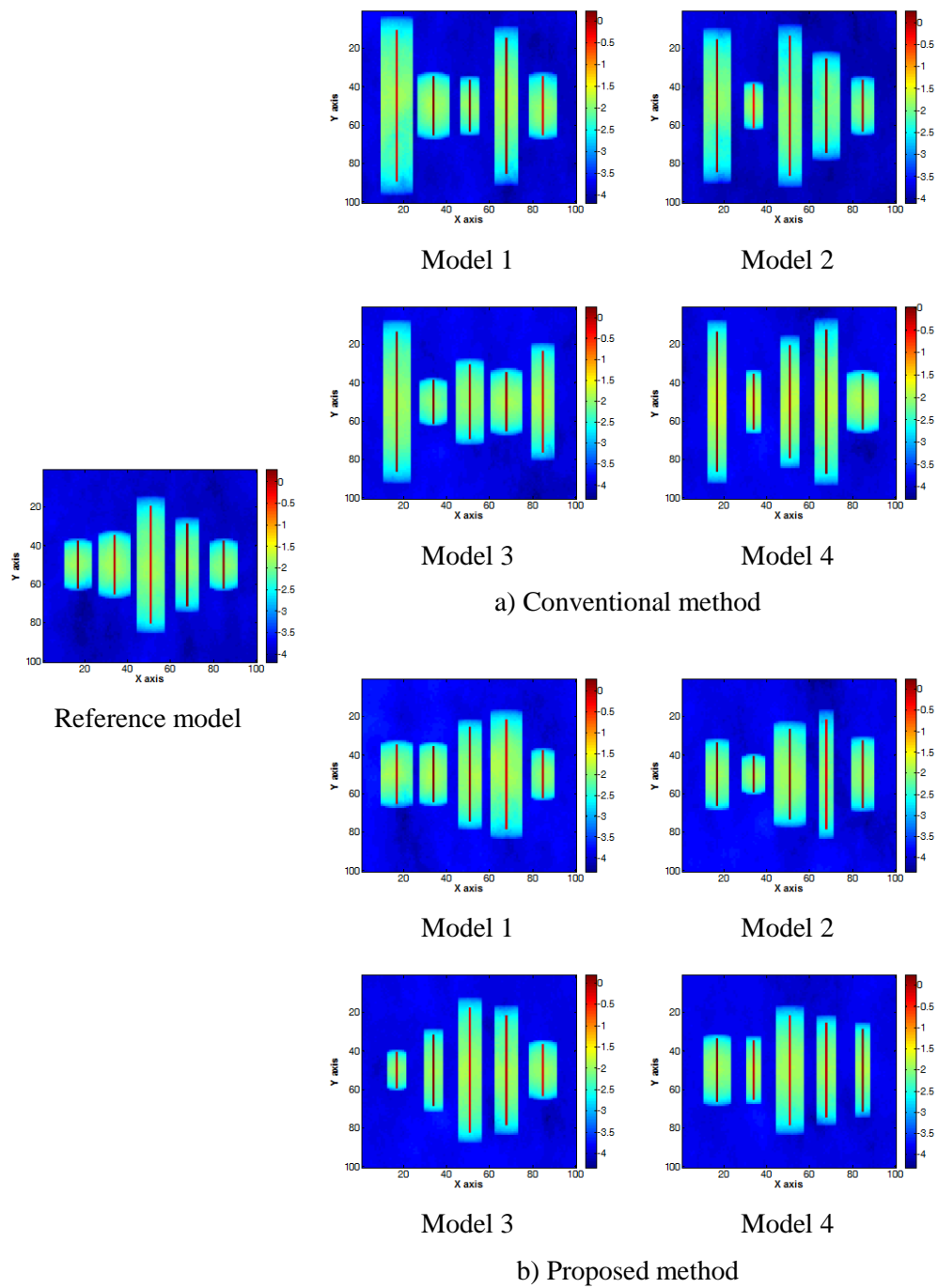Figure A.7 EUR trend versus cluster number with case 1.

Model 1 Model 2

Model 3 Model 4

a) Conventional method

Reference model

Model 1 Model 2

Model 3 Model 4

b) Proposed method

Figure A.8 Log permeability of 4 representative models of conventional and proposed
method with case 1.

Model selection by proposed method with case 2

Table A.3 Results of model selection, first iteration by proposed method with case 2

Cluster number	8	5	7	4	2	6	3	1	Total
# of models	38	34	64	76	59	44	54	31	400
Prob	0.3698	0.2926	0.1795	0.0739	0.0511	0.0182	0.0148	0.0002	
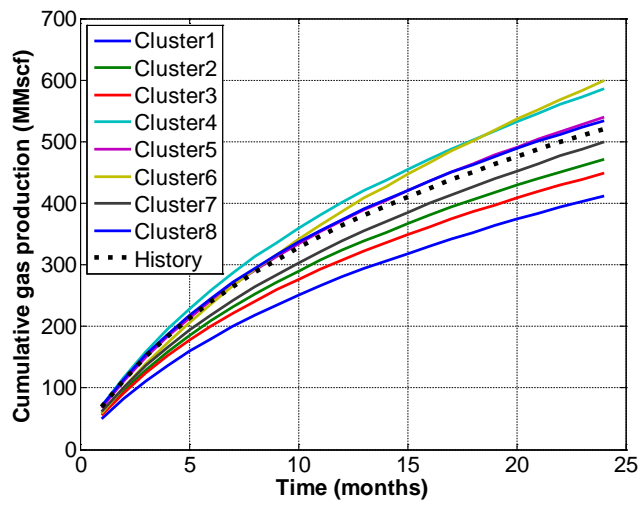
Figure A.9 Comparison of simulation results to actual field data, first iteration by proposed method with case 2.

Table A.4 Results of model selection, second iteration by proposed method with case 2

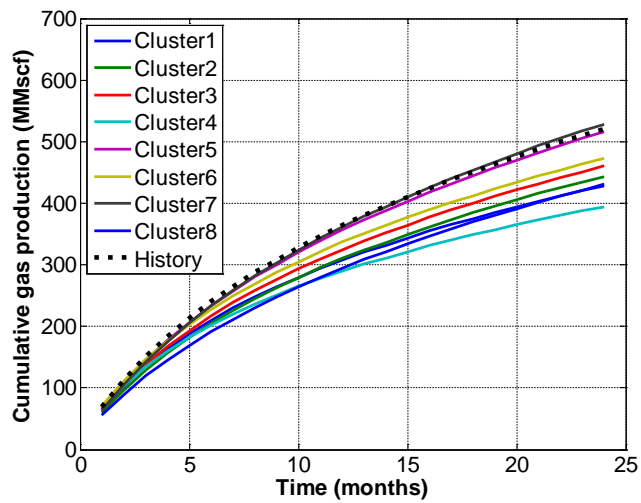| Cluster number	5	3	6	7	1	2	4	8	Total
# of models	12	7	2	3	5	2	2	5	38
Prob	0.4710	0.3359	0.0868	0.0713	0.0260	0.0074	0.0012	0.0003	

Figure A.10 Comparison of simulation results to actual field data, second iteration by proposed method with case 2.
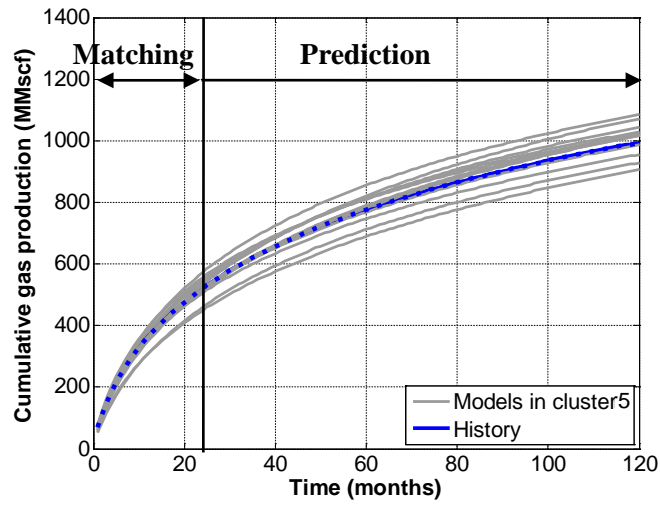
Figure A.11 Cumulative gas production for 10 years by proposed method with case 2.
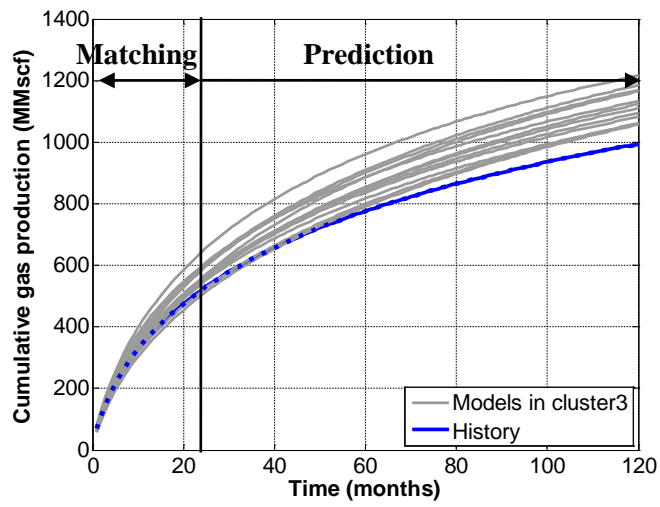
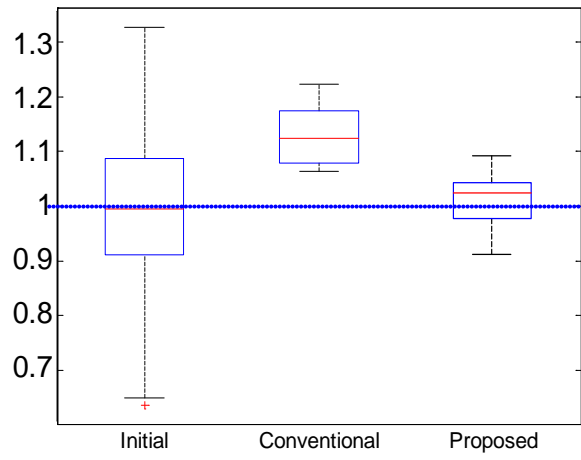Figure A.12 Cumulative gas production for 10 years by conventional method with case 2.

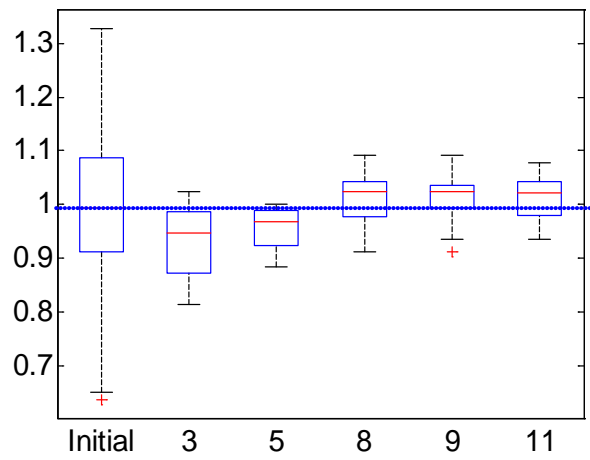Figure A.13 Uncertainty range of EUR at 10 years with case 2.

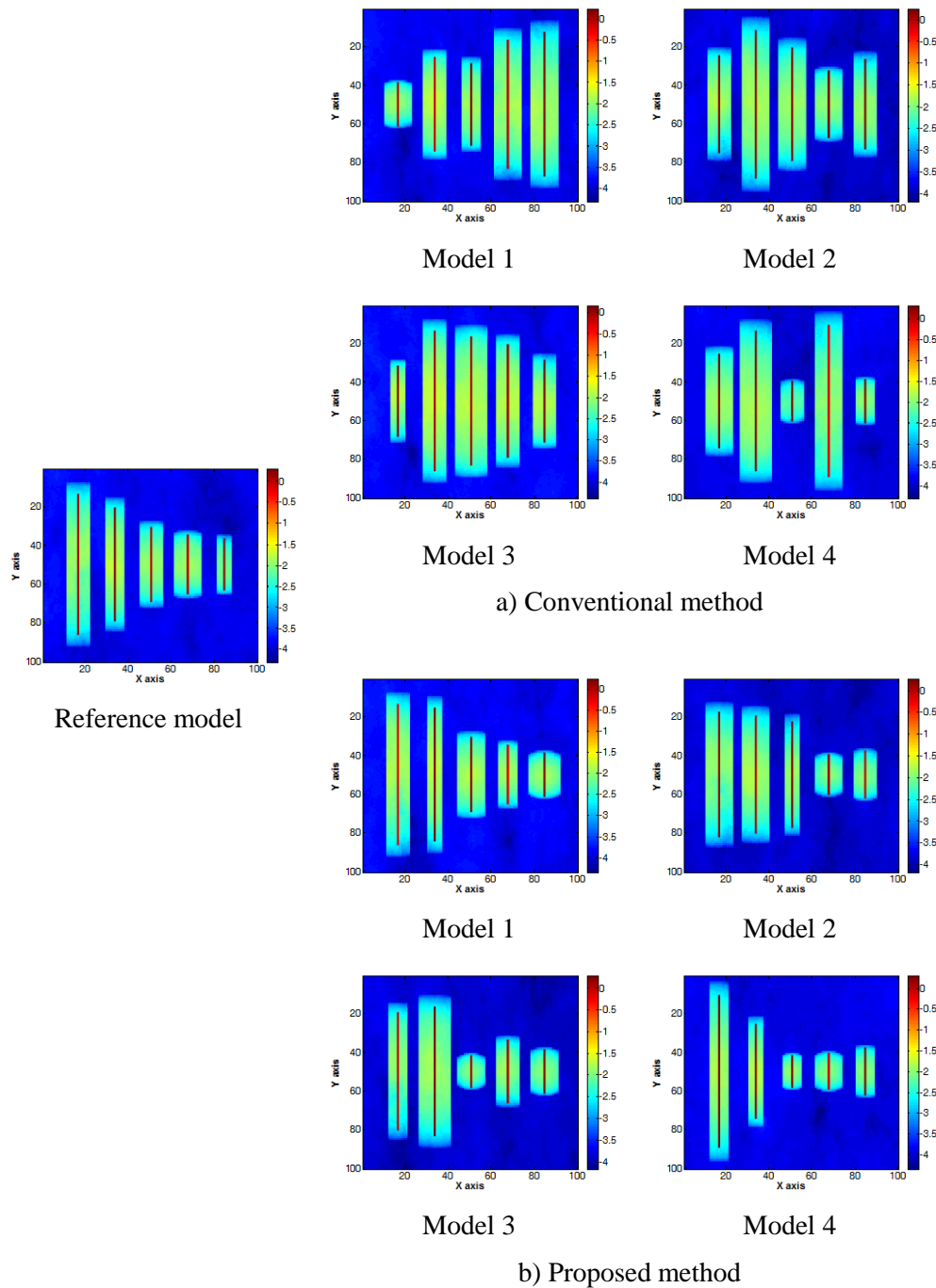Figure A.14 EUR trend versus cluster number with case 2.

Model 1   Model 2

Model 3   Model 4

a) Conventional method

Reference model

Model 1   Model 2

Model 3   Model 4

b) Proposed method

Figure A.15 Log permeability of 4 representative models of conventional and proposed method with case 2.

Model selection by proposed method with case 3

Table A.5 Results of model selection, first iteration by proposed method with case 3

| Cluster number	5	6	3	2	4	7	1	Total
# of models	70	74	43	54	41	82	36	400
Prob	0.7490	0.1405	0.0511	0.0319	0.0151	0.0122	0.0001	
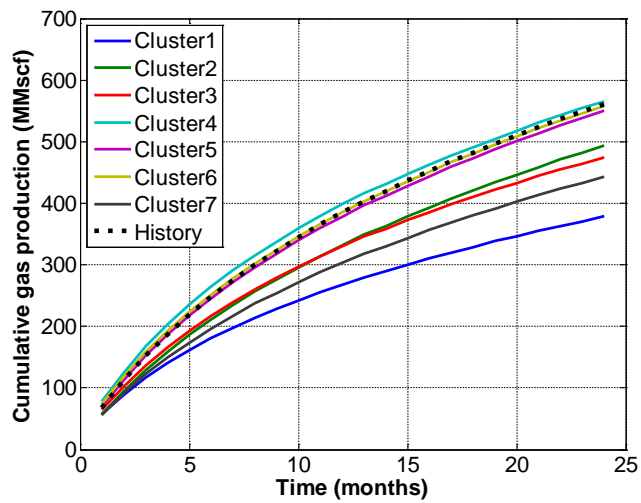
Figure A.16 Comparison of simulation results to actual field data, first iteration by proposed method with case 3.

Table A.6 Results of model selection, second iteration by proposed method with case 3

Cluster number	**5**	4	3	7	2	6	1	Total
# of models	**11**	18	12	8	7	6	8	70
Prob	**0.4335**	0.2650	0.2211	0.0684	0.0086	0.0029	0.0005	
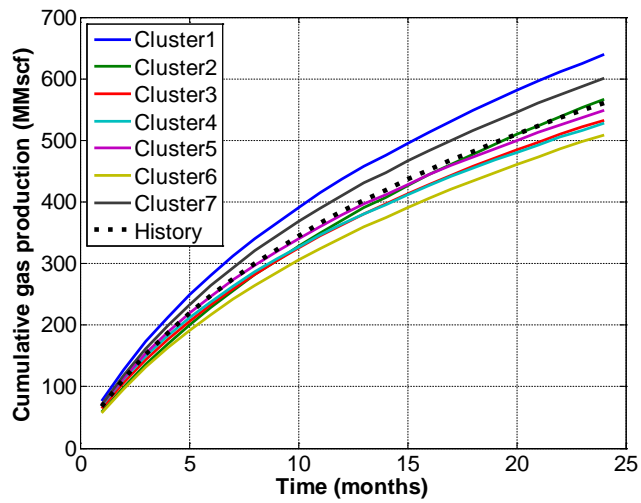
Figure A.17 Comparison of simulation results to actual field data, second iteration by proposed method with case 3.
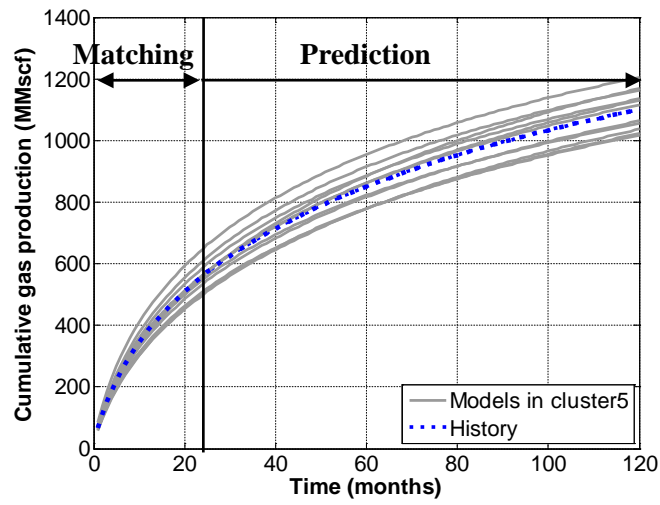
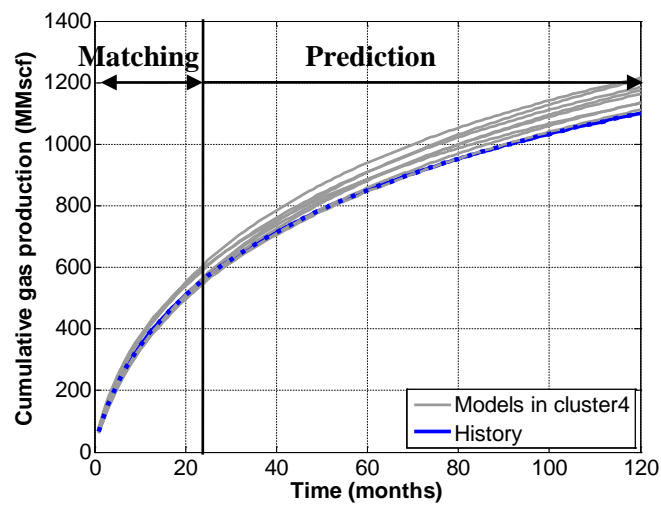Figure A.18 Cumulative gas production for 10 years by proposed method with case 3.

Figure A.19 Cumulative gas production for 10 years by conventional method with case 3.
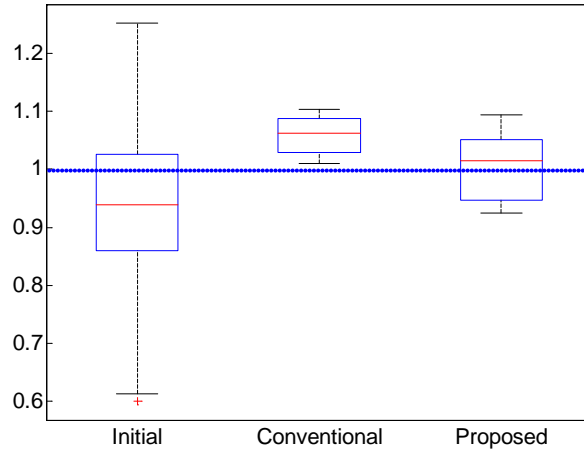
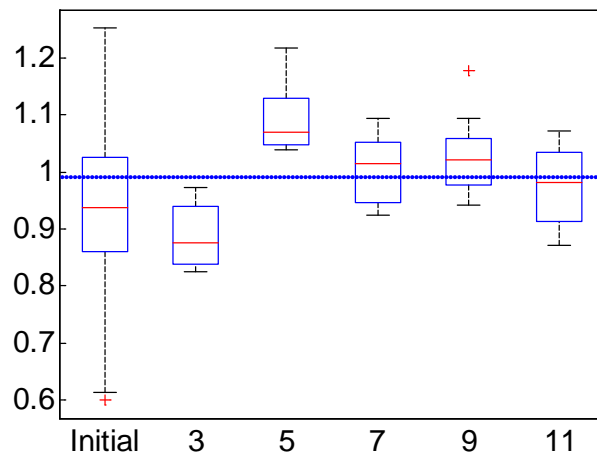Figure A.20 Uncertainty range of EUR at 10 years with case 3.

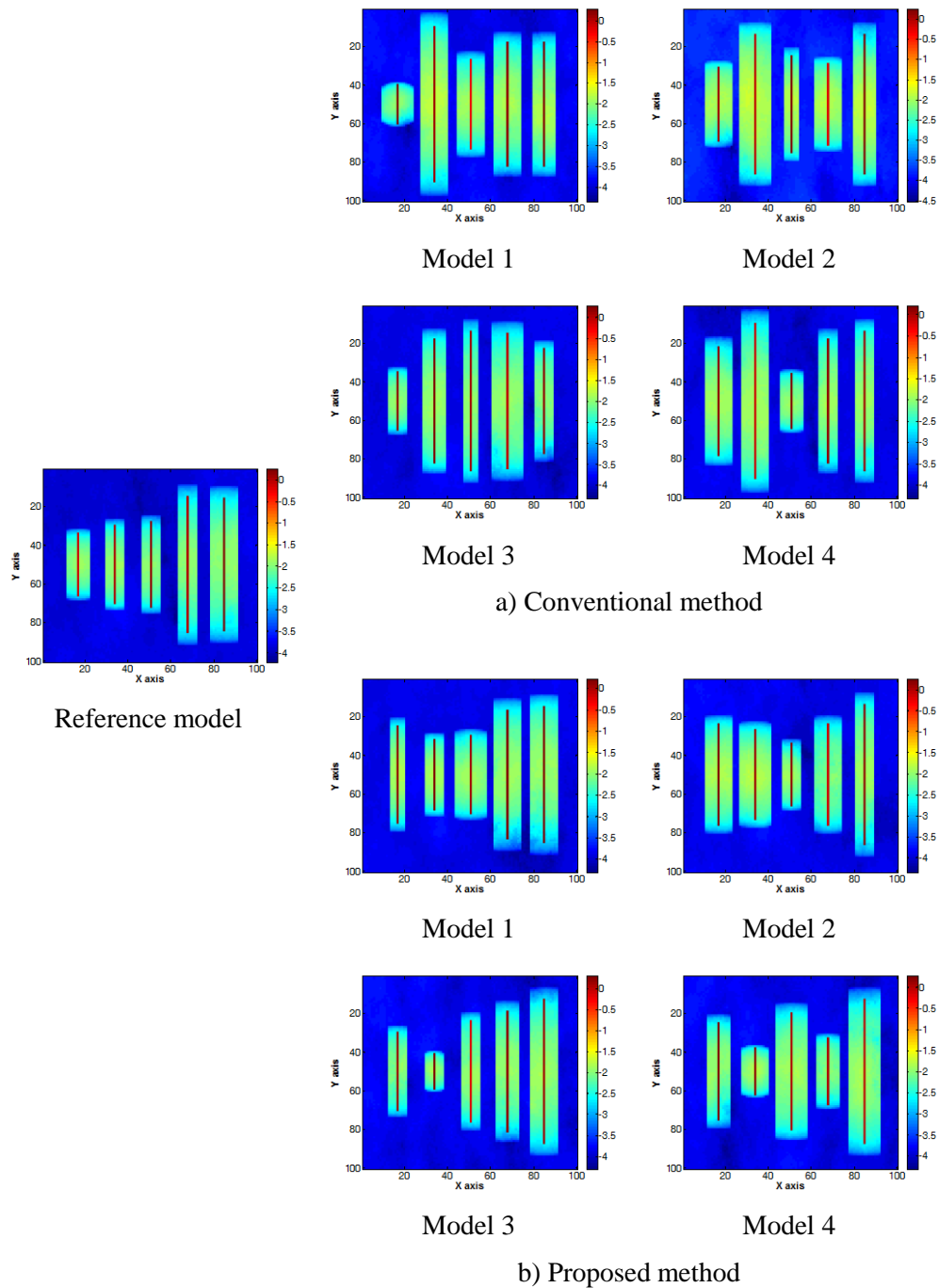Figure A.21 EUR trend versus cluster number with case 3.

Model 1   Model 2

Reference model

Model 3   Model 4

a) Conventional method

Model 1   Model 2

Model 3   Model 4

b) Proposed method

Figure A.22 Log permeability of 4 representative models of conventional and proposed method with case 3.

요약 (국문초록)

셰일가스전은 수압파쇄 운영기법에 따라 다양한 생산특성을 보이기 때문에 향후 생산 예측을 위해서는 특정 셰일가스 저류층에 적합한 특성화가 필요하다. 이를 위해서는 다양한 저류층들을 유사성에 따라 군집화하고, 대상 저류층의 생산자료와 비슷한 거동을 보이는 군집을 선정하는 모델선정법이 필요하다. 그러나 기존 군집화 과정에서 사용하는 균열 반길이, 평균 유체투과율 등의 정적 특성값은 저류층의 동적 연결성을 반영하지 못하여 유사한 특징을 가진 저류층끼리 군집화하지 못하는 한계점이 있다.

본 연구에서는 Fast Marching Method (FMM)를 모델선정법과 결합하여 실제 생산자료와 유사한 거동을 보이는 저류층을 선정하는 기법을 제안하였다. 군집화 과정에 동적 연결성을 반영하기 위해 FMM으로 산정한 유정자극범위를 사용하였다. 또한 제안 기법을 다양한 균열 형태의 가상 저류층을 통해 검증하였다.

본 연구에서 제안된 기법은 유사한 동적자료와 균열 분포를 가지는 저류층의 효과적인 군집화가 가능하였다. 정적 특성값을 이용한 기존 군집화 기법에 비해 약 7–14%p 낮은 오차를 보여 궁극가채량 산출 정확성을 향상시켰다.